Basicity of Mn^{III}-hydroxo Complexes Controls the Thermodynamics of Proton-Coupled Electron Transfer Reactions

Priya Singh,[a] Markell J. A. Lomax,[a] Adedamola A. Opalade,[a] Brandon B. Nguyen,[a] Martin Srnec,[b] and Timothy A. Jackson [a *]

[a] *The University of Kansas, Department of Chemistry and Center for Environmentally Beneficial Catalysis, 1567 Irving Hill Road, Lawrence, KS 66045, USA.*

[b] *J. Heyrovský Institute of Physical Chemistry, The Czech Academy of Sciences, Dolejškova 3, Prague 8 18223, Czech Republic*

*To whom correspondence should be addressed:
Timothy A. Jackson
Phone: (785) 864-3968
taj@ku.edu

Abstract

Several manganese-dependent enzymes utilize Mn^{III}-hydroxo units in concerted proton-electron transfer (CPET) reactions. We recently demonstrated that hydrogen bonding to the hydroxo ligand in the synthetic $[Mn^{III}(OH)(PaPy_2N)]^+$ complex increased rates of CPET reactions compared to the $[Mn^{III}(OH)(PaPy_2Q)]^+$ complex that lacks a hydrogen bond. In this work, we determine the effect of hydrogen bonding on the basicity of the hydroxo ligand and evaluate the corresponding effect on CPET reactions. Both $[Mn^{III}(OH)(PaPy_2Q)]^+$ and $[Mn^{III}(OH)(PaPy_2N)]^+$ react with strong acids to yield Mn^{III}-aqua complexes $[Mn^{III}(OH_2)(PaPy_2Q)]^{2+}$ and $[Mn^{III}(OH_2)(PaPy_2N)]^{2+}$, for which we determined pK_a values of 7.6 and 13.1, respectively. Reactions of the Mn^{III}-aqua complexes with one-electron reductants yielded estimates of reduction potentials, which were combined with pK_a values to give O–H bond dissociation free energies (BDFEs) of 77 and 85 kcal mol^{-1} for the Mn^{II}-aqua complexes $[Mn^{II}(OH_2)(PaPy_2Q)]^+$ and $[Mn^{II}(OH_2)(PaPy_2N)]^+$. Using these BDFEs, we performed an analysis of the thermodynamic driving force for phenol oxidation by these complexes and observed the unexpected result that slower rates are associated with more asynchronous CPET. In addition, reactions of acidic phenols with the Mn^{III}-hydroxo complexes show rates that deviate from the thermodynamic trends, consistent with a change in mechanism from CPET to proton transfer.

Introduction

Manganese-oxygen complexes play critical roles as intermediates in both biological and synthetic catalysts.[1-9] In biology, manganese superoxide dismutase (MnSOD),[10] manganese lipoxygenase (MnLOX),[11-13] class 1b ribonucleotide reductase,[14-15] and the oxygen evolving complex of photosystem II[3] utilize manganese-oxygen intermediates to mediate reactions ranging from the detoxification of free radicals to water splitting. In synthetic chemistry, manganese catalysts that activate H_2O_2 are capable of an impressive array of substrate oxidation reactions, including olefin epoxidation and C–H bond hydroxylation.[16-23] Such reactions can be used in synthetically useful processes, such as the oxidation of methylene C–H bonds in complex molecules[24] and enantioselective lactonization of unactivated C–H bonds.[25]

While the synthetic Mn catalysts are presumed to use high-valent Mn-oxo species for substrate oxidation, the enzymes MnSOD and MnLOX utilize mid-valent Mn^{III}-hydroxo units to oxidize their biological substrates.[8, 10, 26] In the catalytic cycles proposed for these enzymes, the Mn^{III}-hydroxo centers participate in proton-coupled electron-transfer (PCET) reactions, where the Mn^{III} ion accepts an electron and the hydroxo ligand accepts a proton. While such PCET reactions are ubiquitous in biological and synthetic catalysis,[27-32] an understanding of factors that control the rates of such reactions remain a challenge. Although the transfer of an electron and a proton (net hydrogen atom) would seem to be a simple process, there are several distinct pathways by which this reaction can occur. If we define PCET as a broad set of reactions where the conversion from reactants to products involves the transfer of a proton and electron, then there are subclasses where the proton and electron can be transferred in a single step (referred to here as concerted proton-electron transfer, CPET) or in separate steps (electron-proton transfer, ET-PT, or proton-electron transfer, PT-ET). Figure 1 shows a square scheme for a Mn^{III}-hydroxo and Mn^{II}-aqua couple and

a generic H–OR donor. The stepwise processes feature intermediates, which might or might not be observed experimentally, while the concerted process involves proton and electron transfer through a single transition state. A sub-category of asynchronous, or imbalanced, CPET has emerged as a further classification.[33] In some descriptions, an asynchronous process involves more ET or PT character in the transition state (*i.e.*, oxidatively or basic asynchronous processes, respectively).[34-36] Srnec and co-workers defined asynchronicity in terms of the difference in reduction potentials and pK_as of the oxidant (*e.g.,* Mn^{III}-hydroxo) and radical conjugate (*e.g.*, •OR) of the substrate (equation 1).[33] The asynchronicity can also be expressed in terms of the free energies for the electron-transfer and proton-transfer reactions between the oxidant and substrate (ΔG_{ET} and ΔG_{PT}, respectively; see equation 1). The asynchronicity can be combined with the related concept of frustration (σ; see equation 2) and the overall driving force for the CPET step (ΔG_{CPET}) to give an expression for the three-component thermodynamic contribution to the free energy barrier ($\Delta G^{\neq}_{thermo}$; see equation 3).[37] Both asynchronicity and frustration are so-called off-diagonal thermodynamic terms as they arise from the two off-diagonal thermodynamic branches in the thermodynamic cycle (Figure 1), while ΔG_{CPET} is the diagonal thermodynamic term. Asynchronicity and frustration act in opposition, and their effect on the barrier is weighted by a factor of ¼.

$$\eta = \frac{1}{\sqrt{2}} \times \left(\Delta E^{\circ} - \frac{RT}{F} \times \ln(10) \times \Delta \mathrm{p}K_a\right) = -\frac{1}{\sqrt{2}F} \times (\Delta G_{ET} - \Delta G_{PT}) \qquad \text{equation 1}$$

$$\sigma = \frac{1}{\sqrt{2}} \times \left(\Delta E^{\circ} + \frac{RT}{F} \times \ln(10) \times \Delta \mathrm{p}K_a\right) \qquad \text{equation 2}$$

$$\Delta G^{\neq}_{thermo} = \frac{F}{4}(|\sigma| - |\eta|) + \frac{\Delta G_{CPET}}{2} \qquad \text{equation 3}$$

A correlation between higher reorganization energies and more synchronous reactions suggests that asynchronous reactions should have faster rates than synchronous reactions, even at parity of

driving force.[33] Asynchronous, or imbalanced CPET, has been used to explain unusual rate trends in C–H bond oxidation by Co^{III}-oxo,[35] Mn^{IV}-oxo,[38] Ru^{IV}-oxo,[39] and Cu^{III}-O_2CAr complexes,[34] as well as in reactions of 2-fluorenyl benzoates.[40]

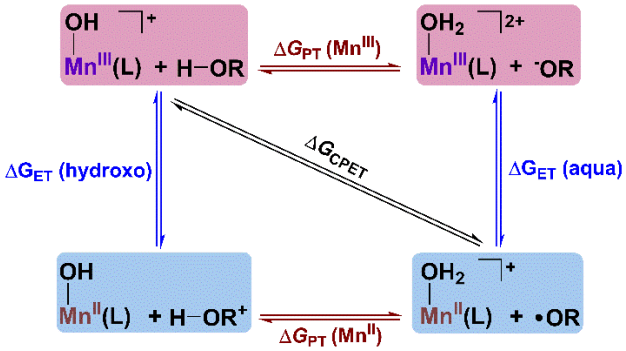

Figure 1. Thermodynamic scheme for PCET reactions with a Mn^{III}-hydroxo / Mn^{II}-aqua couple and a generic H–OR donor. According to this scheme, the ΔG_{ET} and ΔG_{PT} terms in the expressions for asynchronicity and frustration become ΔG_{ET} (hydroxo) and ΔG_{PT} (Mn^{III}).

These classifications notwithstanding, it remains challenging to predict if a given reaction will proceed by a concerted or stepwise process. It is likewise difficult to understand why trends in reaction rates for some systems are well explained on the basis of driving force (*i.e.*, ΔG_{CPET}) alone, while others require consideration of asynchronicity and/ or frustration. Systems that display mechanistic crossover (*i.e.*, from concerted proton-electron transfer to stepwise proton-transfer and electron-transfer) typically involve kinetic investigations for a set of substrates that vary greatly in their acidities and/ or reduction potentials. For example, investigations of the reactions of Cu^{III}-hydroxo complexes with a series of *para*-substituted phenols by Tolman and Mayer revealed a change from a CPET to a PT-ET mechanism for more acidic phenols.[41] Recently, Anderson and co-workers described a similar mechanistic crossover from CPET to PT-ET for reactions of a Co^{III}-oxo complex with *para*-substituted 2,6-di-*t*-butylphenols.[42] In both cases an intermediate was observed in reactions with acidic phenols, which provided evidence for an initial PT step. Alternatively, Hammarström and co-workers have described how plots of reaction rates

versus the driving force for ET, PT, or CPET can be used to identify a reaction type and understand when reaction crossover might occur.[29] These plots rely on accurate values for bond dissociation free energies (BDFEs), reduction potentials, and pK_a values. Similarly, calculations of reaction asynchronicity, whether the Srnec model[33] or the recently proposed semi-empirical model of Borovik and Green,[38] rely on knowledge of these thermodynamic parameters.

Efforts aimed at understanding PCET reactions of Mn^{III}-hydroxo complexes have primarily explored how changes in the environment of the Mn^{III}-hydroxo unit alter reaction rates.[43-49] In one case, the rate of reaction of a set of four Mn^{III}-hydroxo complexes (Figure 2, left) with the hydrogen-atom donor TEMPOH increased as the $Mn^{III/II}$ reduction potential became more positive.[45] The variation in reduction potentials led to corresponding changes in the O–H BDFE in the Mn^{II}-aqua products according to equation 4, such that the Mn^{III}-hydroxo complexes with more positive $Mn^{III/II}$ reduction potentials formed stronger O–H bonds in the Mn^{II}-aqua products.

$$BDFE(\mathrm{O-H}) = 1.37\mathrm{p}K_a(\mathrm{Mn^{II}-OH_2}) + 23.06E^{\circ}(\mathrm{Mn^{III}-OH\ /\ Mn^{II}-OH}) + C_{G,sol}$$

equation 4

(DFT calculations predicted minimal changes in the pK_a values of the Mn^{II}-aqua species.) The net result was a correlation between the reaction rate and the BDFE of the O–H bond formed during the reaction, which is a hallmark of a CPET mechanism. More recently, a similar pair of complexes was employed to examine the role of hydrogen-bonding on treactivity (Figure 2, center and right).[49] In this case, the complex capable of forming an intramolecular hydrogen bond with the hydroxo ligand ($[Mn^{III}(OH)(PaPy_2N)]^+$) showed a rate of TEMPOH oxidation ~16-fold greater than that of the complex lacking the hydrogen bond ($[Mn^{III}(OH)(PaPy_2Q)]^+$).[50] DFT calculations suggested that an increase in basicity for $[Mn^{III}(OH)(PaPy_2N)]^+$ led to a stronger O–H BDFE in the Mn^{II}-aqua product, which accounts for the faster reaction rate. The $[Mn^{III}(OH)(PaPy_2N)]^+$

complex oxidized *para*-substituted 2,6-di-*t*-butylphenols ~65- to 100-fold faster than $[Mn^{III}(OH)(PaPy_2Q)]^+$. The basis for this different rate enhancement was unclear, but it was speculated that the more acidic O–H bonds in the phenol substrates could be a contributing factor. Moreover, the enhanced basicity of $[Mn^{III}(OH)(PaPy_2N)]^+$ relative to $[Mn^{III}(OH)(PaPy_2Q)]^+$ was only inferred from DFT computations.

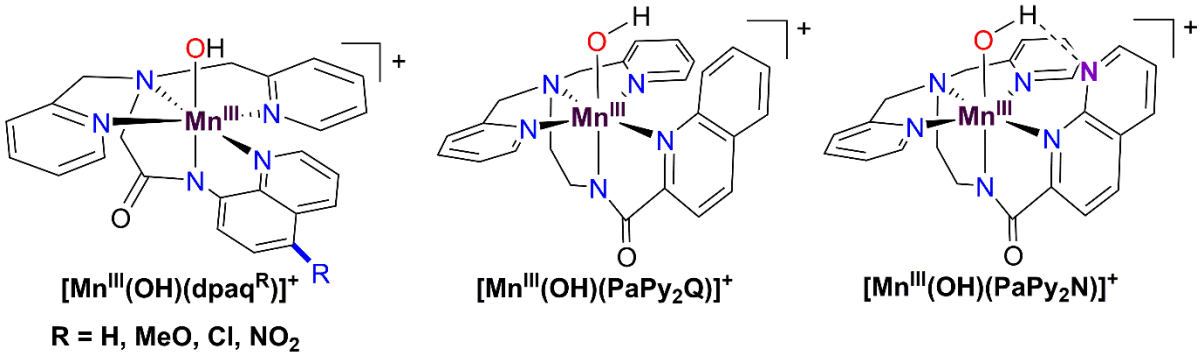

Figure 2. Schematic structures of Mn^{III}-hydroxo complexes.

In this present work, we addressed these issues by experimentally probing the different basicities of $[Mn^{III}(OH)(PaPy_2N)]^+$ and $[Mn^{III}(OH)(PaPy_2Q)]^+$. Titrations of the Mn^{III}-aqua complexes $[Mn^{III}(OH_2)(PaPy_2N)]^{2+}$ and $[Mn^{III}(OH_2)(PaPy_2Q)]^{2+}$ with base yielded O–H pK_a values for the aqua ligands, which show that the hydroxo in $[Mn^{III}(OH)(PaPy_2N)]^+$ is significantly more basic than that of $[Mn^{III}(OH)(PaPy_2Q)]^+$.[49] Reactions of the Mn^{III}-hydroxo complexes with an acidic phenol reveal that increased phenol acidity can change the nature of the reaction from CPET to PT. These results are discussed in light of thermodynamic properties of these reactions.

Experimental and Computational Methods.

Chemicals and HPLC grade solvents were purchased from commercial vendors and used directly without further purification, unless noted. Dried and degassed acetonitrile, methanol, ether, and dichloromethane were obtained from a Pure Solv solvent purification system. Phenols

were purified by recrystallizing from hot ethanol or hexanes. Tetrabutylammonium hexafluorophosphate ($TBAPF_6$) was purified by three recrystallizations from hot ethanol to remove chloride impurities. Protonated dimethylformamide triflate ([H-DMF](OTf)) was prepared by a slight modification of the procedure of Favier and co-workers.[51] Anhydrous DMF (4.7 g; 0.064 mmol) was mixed with 20 mL anhydrous ether in the glovebox. The flask was sealed with a rubber septum before removal from a glovebox and kept under an inert atmosphere using a Schlenk line. Triflic acid (10 g; 0.067 mmol) was added to this solution at 0 °C, and the solution was stirred for 15 minutes. ***Caution!*** *Triflic acid is a strong acid that can cause severe burns and irritation of the respiratory tract. It must be handled with appropriate personal protective equipment and avoid exposure to moist air and water.* The [H-DMF](OTf) product formed as a white precipitate and was isolated by removing ether under vacuum. The purity of [H-DMF](OTf) was determined by ^{1}H NMR spectroscopy. The ligands *N*,*N*-bis(2-pyridinylmethyl)amine-*N*-ethyl-2-quinolinecarboxamide ($PaPy_2QH$)[50] and *N*,*N*-bis(2-pyridinylmethyl)amine-*N*-ethyl-1,8-naphthyridine-2-carboxamide ($PaPy_2NH$) and the [$Mn^{II}(PaPy_2Q)$](OTf) and [$Mn^{II}(PaPy_2N)$](OTf) complexes were synthesized according to reported procedures.[49]

Electronic absorption data were collected on an Agilent 8453 spectrophotometer or a Varian Cary 50 Bio interfaced with a Unisoku cryostat (USP-203-A). ^{1}H NMR data were collected on a Bruker AVIIIHD 400 MHz spectrometer. The raw ^{1}H NMR data were further processed by the MestReNova software.

Formation of Mn^{III}-hydroxo and Mn^{III}-aqua Complexes. Solutions of 1.25 mM [$Mn^{III}(OH)(PaPy_2Q)]^+$ and [$Mn^{III}(OH)(PaPy_2N)]^+$ were made in a nitrogen-filled glovebox by dissolving 15.0 and 16.1 mg of the corresponding Mn^{II} species in 20 mL acetonitrile. Each solution was added to a vial containing 2.8 mg PhIO (0.5 equiv. with respect to Mn^{II} solution) and stirred

overnight. A 2 mL aliquot of each Mn^{III}-hydroxo solution was placed in a quartz cuvette and the cuvette was sealed with a pierceable septum. To the 1.25 mM $[Mn^{III}(OH)(PaPy_2Q)]^+$ solution, 50 μL of a Brönsted acid (1 equiv.), either [H-DMF](OTf) or $HClO_4$, was added at −40 °C to form the $[Mn^{III}(OH_2)(PaPy_2Q)]^{2+}$ complex. The low temperature was required due to the low thermal stability of $[Mn^{III}(OH_2)(PaPy_2Q)]^{2+}$. Similarly, a 50 μL aliquot of acid was added to a 1.25 mM solution of $[Mn^{III}(OH)(PaPy_2N)]^+$ at −40 °C to form $[Mn^{III}(OH_2)(PaPy_2N)]^{2+}$ complex. In this case, the Mn^{III}-aqua complex was more thermally stable, and this reaction could also be performed at 25 °C. The changes in the electronic absorption spectra upon the addition of acid to the solutions of Mn^{III}-hydroxo species were monitored by UV-vis spectroscopy. The Mn^{III}-aqua complexes were further characterized by ^{1}H NMR spectroscopy (*vide infra*), and magnetic moments of 5.0 μ_B were determined for both Mn^{III}-aqua complexes in CD_3CN by the Evan's method. The stabilities of the Mn^{III}-aqua complexes were determined by monitoring their electronic absorption bands at 25 °C in acetonitrile.

^{1}H-NMR Experiments for the Mn^{III}-aqua Complexes. 15 mM solutions of $[Mn^{III}(OH)(PaPy_2Q)]^+$ and $[Mn^{III}(OH)(PaPy_2N)]^+$ were prepared using the protocol described previously in 0.4 ml of CD_3CN. Once maximum formation of the Mn^{III}-hydroxo complexes was achieved, as confirmed from the UV-vis spectroscopy, the solution temperature was dropped to −40 °C, and a 100 μL aliquot of CD_3CN delivering 1 equiv. acid was added to each solution to give a final volume of 0.5 mL. The ^{1}H NMR spectra of both $[Mn^{III}(OH_2)(PaPy_2Q)]^{2+}$ and $[Mn^{III}(OH_2)(PaPy_2N)]^{2+}$ complexes were collected at -40 °C in deuterated acetonitrile using the wide scan range of 200 to −150 ppm, a relaxation time of zero, and 1024 scans. The ^{1}H NMR spectrum for $[Mn^{III}(OH_2)(PaPy_2N)]^{2+}$ was also collected at 25 °C in CD_3CN.

Titration of Mn^{III}-aqua Complexes with Brønsted Bases. A 0.5 mM solution of $[Mn^{III}(OH_2)(PaPy_2Q)]^{2+}$ was titrated against *p*-cyanopyridine (4 to 20 equiv. relative to total Mn concentration; pK_a = 8.10) in acetonitrile at −40 °C and monitored by UV-vis spectroscopy. After each increment of base was added, the concentrations of the Mn^{III}-hydroxo and Mn^{III}-aqua species were determined from a two-component spectral deconvolution. The concentrations of *p*-cyanopyridine and its conjugate base were determined by mass balance, and an equilibrium constant was calculated for each equivalent of base added. This process was repeated twice to determine the pK_a for $[Mn^{III}(OH_2)(PaPy_2Q)]^{2+}$. A similar procedure was employed to determine the pK_a for $[Mn^{III}(OH_2)(PaPy_2N)]^{2+}$ but using pyridine as base (0.25 mM – 2.0 mM; pK_a = 12.53).

Determination of Reduction Potentials (E_{red}) of Mn^{III}-aqua Complexes. The range of $Mn^{III/II}$ reduction potentials of the Mn^{III}-aqua complexes was determined by chemically reducing the Mn^{III}-aqua species by employing several one-electron reducing agents. A solution of 1.25 mM $[Mn^{III}(OH_2)(PaPy_2Q)]^{2+}$ was reacted with 1 equiv. ferrocene (0.0 V vs. Fc/Fc^+), 1,1′-dibromoferrocene (0.35 V vs. Fc/Fc^+), 1,1′-diacetylferrocene (0.46 V vs. Fc/Fc^+), *p*-bromo-*N*,*N*-dimethylaniline ($E_{1/2}$ = 0.55 V vs. $Fc^{+/0}$), or tris(4-bromophenyl)ammoniumyl hexachloroantimonate (0.67 V vs Fc/Fc^+) in acetonitrile and the reactions were monitored using UV-vis spectroscopy. A similar procedure was followed to determine the range of the reduction potential of $[Mn^{III}(OH_2)(PaPy_2N)]^{2+}$ complex in acetonitrile. A control reaction was also performed where 1.25 mM Mn^{III}-hydroxo complexes were reacted with each of the reducing agents in acetonitrile. Although we attempted to determine the potentials of the Mn^{III}-aqua complexes using cyclic voltammetry, these experiments did not yield peaks that we could reliably attribute to the $Mn^{III/II}$-aqua couple.

Kinetic Experiments for Reactions of Mn^{III}-hydroxo Complexes with 4-NO_2-2,6-di-tert-butylphenol. A quartz cuvette of 2 mL of a 1.25 mM MeCN solution of the Mn^{III}-hydroxo complex ($[Mn^{III}(OH)(PaPy_2Q)]^+$ or $[Mn^{III}(OH)(PaPy_2N)]^+$) was prepared and sealed with a pierceable septum. The cuvette was placed in a spectrometer with a temperature controller set to 50 °C. An excess of substrate (4-NO_2-2,6-di-*t*-butyphenol), dissolved in 200 μL of degassed dichloromethane, was added to the cuvette through the septum. The decay of the absorption features of the Mn^{III}-hydroxo complex was monitored by UV-vis spectroscopy. This decay was fit to a first-order model to obtain observed rates (k_{obs}). This procedure was performed for different concentrations of substrate (20 mM – 50 mM). Second-order rate constants were obtained from the slope of plots of k_{obs} versus substrate concentration. Additional experiments were performed to explore the reactivity of the Mn^{III}-hydroxo complexes with the acidic phenols 4-bromo-2,6-di-*t*-butyphenol and 4-methoxycarbonyl-2,6-di-*t*-butyphenol. However, the kinetics for these reactions were complex and could not be readily analyzed by the kinetic model used for the other phenols. Thus, we did not pursue these reactions further.

Computational Methods. Calculations were performed using the *ORCA* 5.0.3 software package.[52-53] Structures of the $[Mn^{III}(OH_2)(PaPy_2Q)]^{2+}$, $[Mn^{III}(OH_2)(PaPy_2N)]^{2+}$, and $[Mn^{III}(OH)(PaPy_2NH)]^{2+}$ were optimized using the B3LYP-D3 functional[54-55] with def2-TZVP basis sets for Mn, O, and N and def2-SVP for C and H.[56-57] The RIJCOSX approximation was used to speed up the calculations, and an appropriate auxiliary basis set was called using the AutoAux command.[58] Optimized geometries were verified to be a minimum through frequency calculations at the same level of theory. For single point energy calculations, we used the larger def2-TZVPP basis set for all atoms. Time-dependent DFT (TD-DFT) calculations were performed using the same basis sets employed in the geometry optimization, except an auxiliary def2-

TZVP/C basis set was used, and solvent effects were incorporated using an SMD solvation model for acetonitrile.[59] The TD-DFT electronic absorption spectra were generated by modeling each electronic transition as a Gaussian band with a full-width-at-half-maximum of 2500 cm^{-1}. Isosurface plots of Kohn-Sham molecular orbitals were visualized using the Chemcraft software. Net thermodynamics for reactions of the Mn^{III}-aqua complexes and phenols were calculated by two approaches, which are described in the Supplementary Information. In one approach, we used the experimental thermodynamic parameters for the Mn complexes and calculated parameters for the phenols.

Results and Discussion.

Reaction of Mn^{III}-hydroxo Complexes with Acid. In order to determine any differences in the basicity of $[Mn^{III}(OH)(PaPy_2Q)]^+$ and $[Mn^{III}(OH)(PaPy_2N)]^+$, we first used electronic absorption spectroscopy to explore the reactions of these complexes with Brønsted acids. The reaction of $[Mn^{III}(OH)(PaPy_2Q)]^+$ with 1.0 equiv. [H-DMF](OTf) in MeCN at -40 °C resulted in the formation of a new species with features at 430, 650, and 1000 nm (Figure 3, top). This reaction proceeded with isosbestic points at 480, 577, 726, and 875 nm, indicating a reaction without any accumulating intermediates. The formation of this new species was also observed upon the addition of 1 equiv. $HClO_4$ to $[Mn^{III}(OH)(PaPy_2Q)]^+$ (Figure S1). When pyridine (1 equiv.) was added to the same solution, the new chromophore reverted to the initial $[Mn^{III}(OH)(PaPy_2Q)]^+$ complex (95% recovery on the basis of the absorption intensity; see Figure S1). This reversibility suggests that the new species is a protonated product of $[Mn^{III}(OH)(PaPy_2Q)]^+$. In addition, this new species displays a magnetic moment in solution of 5.0 μ_B (Figure S2), which is consistent

with that expected for a high-spin ($S = 2$) Mn^{III} center (4.9 μ_B). Thus, the addition of acid does not change the oxidation state or nuclearity of the complex.

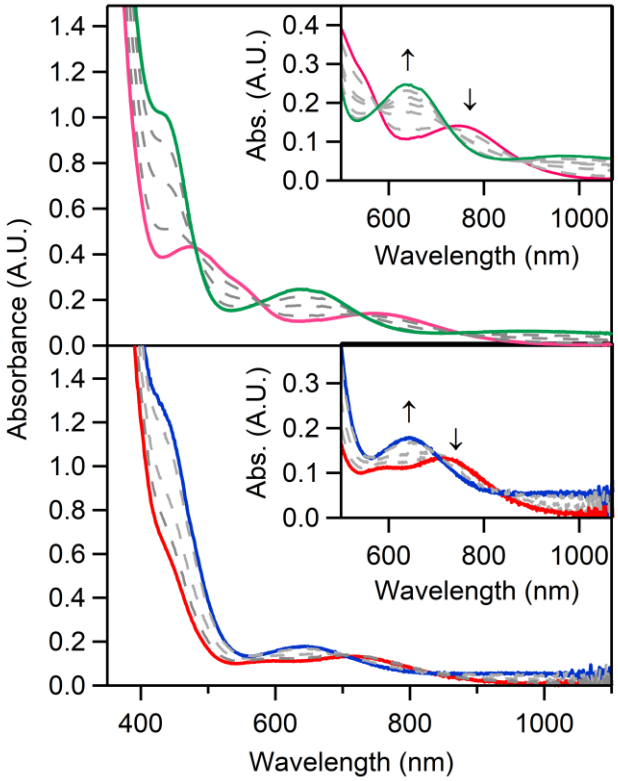

Figure 3. Top: Electronic absorption spectra showing the reaction of 1 mM $[Mn^{III}(OH)(PaPy_2Q)]^+$ (pink) with 1 equiv. [H-DMF](OTf) to give $[Mn^{III}(OH_2)(PaPy_2Q)]^{2+}$ (green) in MeCN at -40 °C. Bottom: Electronic absorption spectra showing the reaction of 1 mM $[Mn^{III}(OH)(PaPy_2N)]^+$ (red) with 1 equiv. [H-DMF](OTf) to give $[Mn^{III}(OH_2)(PaPy_2N)]^{2+}$ (blue) in MeCN at 25 °C. The insets show an expanded view of the low-energy spectral region during the reactions.

Similar reactivity with acid was observed for $[Mn^{III}(OH)(PaPy_2N)]^+$. The addition of 1 equiv. [H-DMF](OTf) or $HClO_4$ to a solution of $[Mn^{III}(OH)(PaPy_2N)]^+$ in MeCN at 25 °C led to the growth of a shoulder at 430 nm and the appearance of the new bands at 640 and 1000 nm (Figure 3, bottom, and Figure S3). These reactions could be reversed by the addition of 1 equiv. triethylamine to give the initial $[Mn^{III}(OH)(PaPy_2N)]^+$ complex in 96% yield (Figure S3). The reaction product showed a magnetic moment in solution of 5.0 μ_B (Figure S2), consistent with a high-spin, mononuclear Mn^{III} center. While the product formed after the addition of acid to

$[Mn^{III}(OH)(PaPy_2Q)]^+$ had limited stability at 25 °C ($t_{1/2}$ = 200 s), the product formed after the addition of acid to $[Mn^{III}(OH)(PaPy_2N)]^+$ was quite stable at 25 °C ($t_{1/2} \approx 4200$ s).

To aid in understanding the structures of the protonated forms of $[Mn^{III}(OH)(PaPy_2Q)]^+$ and $[Mn^{III}(OH)(PaPy_2N)]^+$, we compared the spectral changes observed here to those of the related $[Mn^{III}(OH)(dpaq)]^+$ complex (Figure 2).[60-61] In that case, crystallographic and spectroscopic data established the protonated product as the Mn^{III}-aqua complex $[Mn^{III}(OH_2)(dpaq)]^{2+}$.[14] Given the similarities between the dpaq and $PaPy_2Q$ ligands, this comparison is informative. The electronic absorption spectrum of $[Mn^{III}(OH_2)(dpaq)]^+$ had band maxima at 410, 720, and 1150 nm at 25 °C in acetonitrile, which are very similar to those of the protonated products of $[Mn^{III}(OH)(PaPy_2Q)]^+$ and $[Mn^{III}(OH)(PaPy_2N)]^+$ (430, ~650, and 1000 nm). Based on these similarities, and additional data discussed below, we propose that the $[Mn^{III}(OH)(PaPy_2Q)]^+$ and $[Mn^{III}(OH)(PaPy_2N)]^+$ complexes react with acid to give the corresponding Mn^{III}-aqua species (Scheme 1).

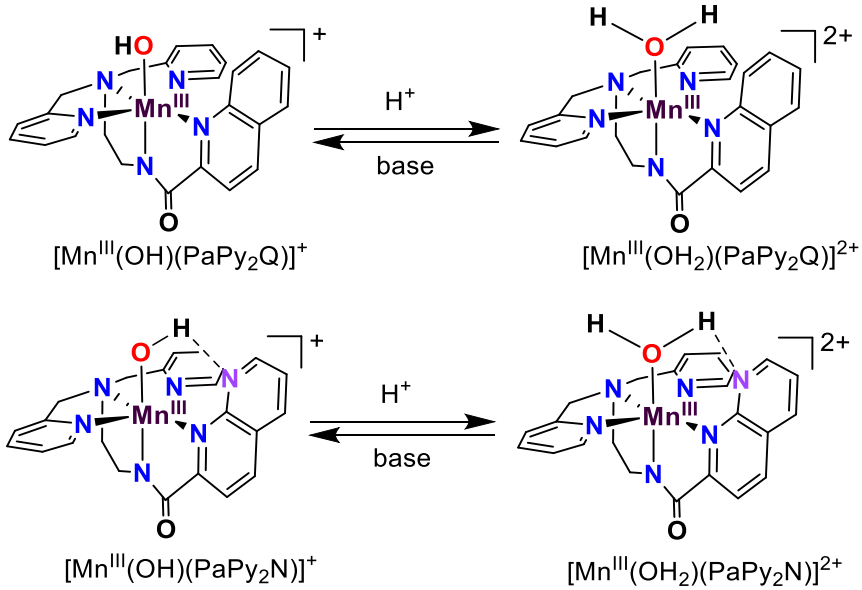

$[Mn^{III}(OH)(PaPy_2Q)]^+$ $[Mn^{III}(OH_2)(PaPy_2Q)]^{2+}$

$[Mn^{III}(OH)(PaPy_2N)]^+$ $[Mn^{III}(OH_2)(PaPy_2N)]^{2+}$

Scheme 1. Reactions of Mn^{III}-hydroxo complexes with acid in acetonitrile.

Comparison of ^{1}H NMR Spectra for Mn^{III}-aqua and Mn^{III}-hydroxo Complexes. We used ^{1}H NMR spectroscopy to further probe the products of the reactions of acid with

$[Mn^{III}(OH)(PaPy_2Q)]^+$ and $[Mn^{III}(OH)(PaPy_2N)]^+$. Although ^1H NMR spectra for $[Mn^{III}(OH)(PaPy_2Q)]^+$ and $[Mn^{III}(OH)(PaPy_2N)]^+$ in the presence of acid cannot provide unambiguous information about the site of protonation, the data can be used to determine if protonation leads to major structural rearrangements, as might be expected if the amide group of the supporting ligand were the site of protonation.

The ^1H NMR spectra of $[Mn^{III}(OH_2)(PaPy_2Q)]^{2+}$ and $[Mn^{III}(OH_2)(PaPy_2N)]^{2+}$ (Figure 4) each show five peaks in the downfield region (~170 to 30 ppm) and three peaks in upfield region (-10 to -120 ppm). The number of peaks and pattern of downfield and upfield peaks matches that previously reported for the Mn^{III}-hydroxo complexes (see Supporting Information),[49] which strongly suggests that there has not been a major perturbation in the binding mode of the $PaPy_2Q$ or $PaPy_2N$ ligands upon protonation. The upfield region of the ^1H NMR spectra for the Mn^{III}-aqua complexes shows modest shifts of less than 20 ppm in peak position relative to the Mn^{III}-hydroxo complexes (Figure 4 and Table 1). Two peaks in this region were tentatively attributed to quinolyl protons for the Mn^{III}-hydroxo complexes.[49] Minor perturbations are also observed in the downfield region of the ^1H NMR spectra of the Mn^{III}-aqua complexes. In each case, a set of two sharper peaks is retained and shifted by only ~10 ppm relative to the Mn^{III}-hydroxo complexes (Figure 4 and Table 1). The three broader, downfield peaks, which appear at ~140, 120, and 45 ppm for the Mn^{III}-hydroxo complexes have shifted to ~160, 80, and 40 ppm for the Mn^{III}-aqua complexes. Taken together, while there are clear shifts in the positions of proton resonances upon protonation of the $[Mn^{III}(OH)(PaPy_2Q)]^+$ and $[Mn^{III}(OH)(PaPy_2N)]^+$ complexes, most shifts are ~10 – 20 ppm, and, importantly, the number and pattern of peaks is unchanged for the protonated complexes.

Table 1. ^1H NMR Chemical Shifts (ppm) for $[Mn^{III}(OH)(L)]^+$ and $[Mn^{III}(OH_2)(L)]^{2+}$ complexes in CD_3CN at different temperatures (L = $PaPy_2Q$ and $PaPy_2N$).

L = PaPy2Q	L = $PaPy_2N$

$[Mn^{III}(OH)(L)]^{+}$		$[Mn^{III}(OH_2)(L)]^{2+}$	$[Mn^{III}(OH)(L)]^{+}$		$[Mn^{III}(OH_2)(L)]^{2+}$
25 °C[a,b]	−40 °C	−40 °C	25 °C[a]	−40 °C	−40 °C
116.4	140.8	157.7	121.7	145.6	166.6
88.7	115	82.1	97.3	124.1	78.7
44.8	52.3	62.6	47.0	54.8	66.9
40.8	47.5	57.4	42.4	49.6	63.6
		41.9	37.4	45.2	33.4
−6.7	−9.6	−13.3	−3.2	−5.0	−11.1
−22.8	−27.3	−34.3	−28.8	−35.2	−41.0
−77.0	−99.0	−116.7	−84.5	−106.3	−122.5

[a] From ref [49]. [b] An eight proton resonance was resolved upon the addition of a small amount of water, which caused the resolution of two-overlapping peaks.

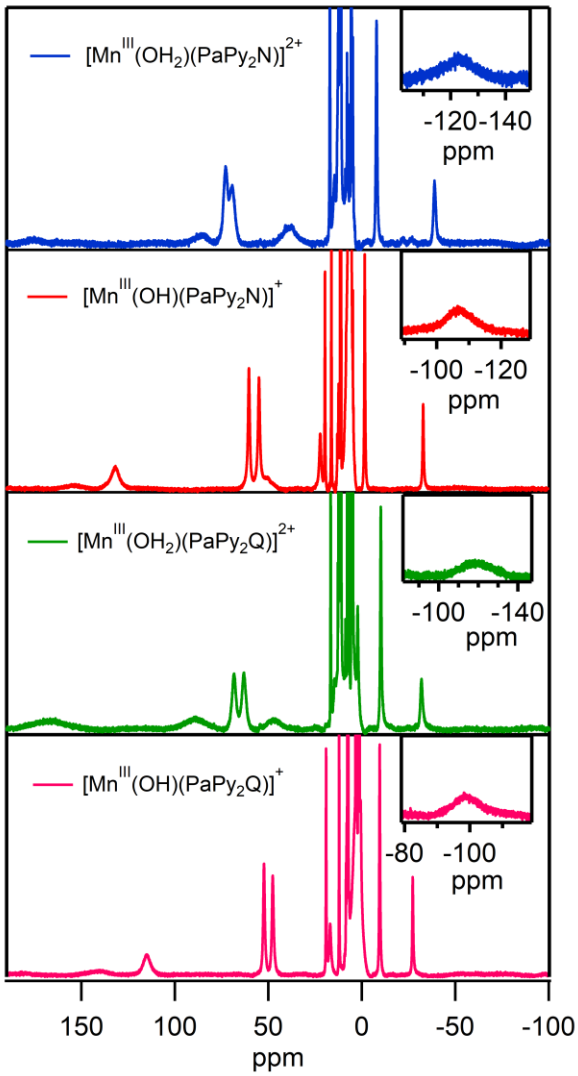

Figure 4. ^{1}H NMR spectra (-40 °C) of 15 mM $[Mn^{III}(OH)(PaPy_2Q)]^{+}$ (pink), $[Mn^{III}(OH)(PaPy_2N)]^{+}$ (red) complexes and their corresponding aqua complexes, $[Mn^{III}(OH_2)(PaPy_2Q)]^{2+}$ (green) and $[Mn^{III}(OH_2)(PaPy_2N)]^{2+}$ (blue), formed after addition of 1 equiv. $HClO_4$.

Evaluation of Mn^{III}-aqua Complexes using DFT computations. To further evaluate our formulations for the $[Mn^{III}(OH_2)(PaPy_2Q)]^{2+}$ and $[Mn^{III}(OH_2)(PaPy_2N)]^{2+}$ complexes, we developed structures using DFT computations and predicted the electronic absorption spectra of these complexes using TD-DFT computations. The Mn–OH_2 bond lengths in $[Mn^{III}(OH_2)(PaPy_2Q)]^{2+}$ and $[Mn^{III}(OH_2)(PaPy_2N)]^{2+}$ are nearly 0.2 Å longer than the Mn–OH bond lengths in the corresponding Mn^{III}-hydroxo complexes (Table 2).[49] The Mn–N2 bond that is

trans to the aqua ligand has contracted by ~0.07 Å relative to the Mn^{III}-hydroxo complexes. Thus, protonation of the hydroxo ligand is accompanied by large changes in both the Mn–O distance and in the *trans* Mn–N2 distance. The remaining Mn–N ligand bond lengths show only minor changes between the Mn^{III}-hydroxo and Mn^{III}-aqua complexes. Even with the elongations of the Mn–OH_2 distances, these complexes retain the same $(3d_{yz})^1(3d_{xy})^1(3d_{xz})^1(3d_{x^2-y^2})^1(3d_{z^2})^0$ configuration that we previously described for the Mn^{III}-hydroxo complexes (Figure S5).[49]

We also explored a potential structure of the protonated form of $[Mn^{III}(OH)(PaPy_2N)]^+$ where the 1,8-naphthyridine moiety is protonated rather than the hydroxo ligand ($[Mn^{III}(OH)(PaPy_2NH)]^{2+}$). As shown by Borovik and co-workers, care must be taken when assigning protonation sites for transition-metal complexes.[63] In the structure of $[Mn^{III}(OH)(PaPy_2NH)]^{2+}$, the N–H unit of the ligand donates a hydrogen bond to the hydroxo ligand (Figure 5, bottom). The metal-ligand bond lengths for $[Mn^{III}(OH)(PaPy_2NH)]^{2+}$ are quite similar to those of $[Mn^{III}(OH)(PaPy_2N)]^+$, with a notable difference being a slight elongation (0.05 Å) of the Mn–OH distance due to the hydrogen bond. A comparison of energies of the $[Mn^{III}(OH_2)(PaPy_2N)]^{2+}$ and $[Mn^{III}(OH)(PaPy_2NH)]^{2+}$ reveals that the latter is lower in energy by 1.9 kcal mol^{-1}. Given the expected accuracy of DFT calculations for transition-metal complexes, we view it as unwise to determine the site of protonation using solely this small DFT energy difference.

Table 2. Selected Bond Lengths (Å) and Angles (°) for Mn^{III}-hydroxo and Mn^{III}-aqua Complexes from X-ray Crystallography and DFT Computations.

	$[Mn^{III}(L)(PaPy_2Q)]^{n+}$ [a]			$[Mn^{III}(L)(PaPy_2N)]^{n+}$ [a]		$[Mn^{III}(OH)(PaPy_2NH)]^{2+}$
	L = OH		L = OH_2	L = OH	L = OH_2	
	XRD[b]	DFT[b]	DFT	DFT[b]	DFT	DFT
Mn–O1	1.8180(16)	1.843	2.034	1.822	1.992	1.873
Mn–N1	2.1945(19)	2.211	2.159	2.172	2.129	2.181
Mn–N2	1.9680(18)	1.956	1.882	1.970	1.896	1.943
Mn–N3	2.2415(19)	2.260	2.219	2.261	2.238	2.267
Mn–N4	2.171(2)	2.166	2.152	2.191	2.159	2.127

Mn–N5	2.138(2)	2.136	2.179	2.161	2.190	2.160
OH···N				1.952	1.539	
O···HN						1.642
N2–Mn–O	174.21	176.2	172.1	176.7	174.0	173.2

[a] For these complexes, n = 1 for L = OH and n = 2 for L = OH_2. [b] From ref. [49].

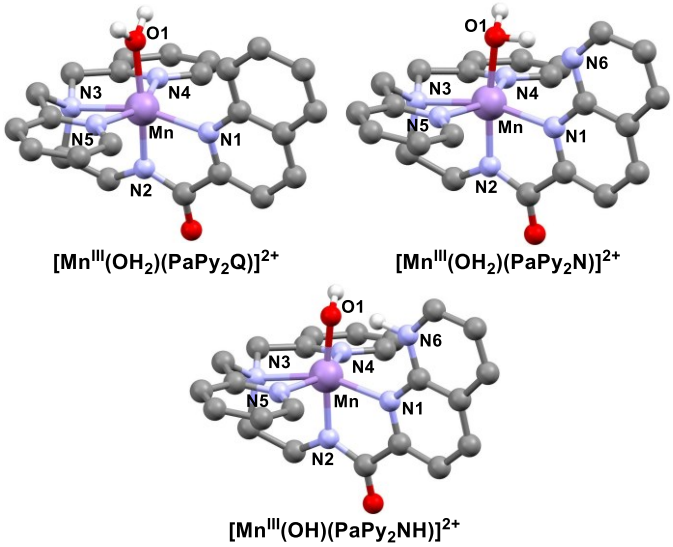

Figure 5. Structures of Mn^{III}-aqua complexes $[Mn^{III}(OH_2)(PaPy_2Q)]^{2+}$ and $[Mn^{III}(OH_2)(PaPy_2N)]^{2+}$ (top) and Mn^{III}-hydroxo complex $[Mn^{III}(OH)(PaPy_2NH)]^{2+}$ (bottom) from DFT computations.

As a further means of evaluating these structures, we used TD-DFT calculations to predict electronic absorption spectra. The TD-DFT-predicted electronic absorption spectra of $[Mn^{III}(OH_2)(PaPy_2Q)]^{2+}$ and $[Mn^{III}(OH_2)(PaPy_2N)]^{2+}$ are quite similar, each showing a weak absorption band in the near-IR region (~1000 – 1200 nm), a more prominent band at ~600 – 700 nm, and the onset of more intense features at wavelengths less than 500 nm (Figure 6). These calculated features nicely match the experimental absorption spectra, and any discrepancies are well within the expected accuracy of the TD-DFT method.[64] In contrast, the TD-DFT electronic absorption spectrum of $[Mn^{III}(OH)(PaPy_2NH)]^{+}$ has one feature at ~810 nm and the onset of intensity at wavelengths less than 600 nm Figure 6, right), in poor agreement with the two experimental bands at 1054 and 620 nm. Thus, the TD-DFT computations for the Mn^{III}-aqua

complex $[Mn^{III}(OH_2)(PaPy_2N)]^+$ better reproduce the experimental data, and we therefore favor this complex.

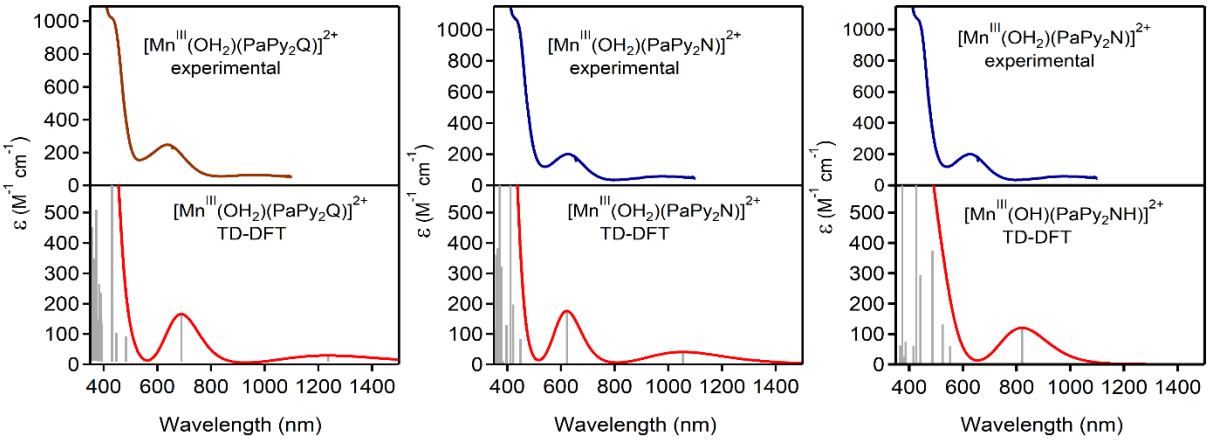

Figure 6. Experimental and TD-DFT computed electronic absorption spectra for $[Mn^{III}(OH_2)(PaPy_2N)]^{2+}$ (left) and $[Mn^{III}(OH_2)(PaPy_2Q)]^{2+}$ (right). The sticks indicate electronic transitions.

pK_a Values and Reduction Potentials of Mn^{III}-aqua Complexes. To determine a pK_a value for the Mn^{III}-aqua complex $[Mn^{III}(OH_2)(PaPy_2Q)]^{2+}$, we performed spectrophotometric titrations with *p*-cyanopyridine (pK_a = 8.1) at −40 °C (Scheme 2). The addition of various concentrations of *p*-cyanopyridine to $[Mn^{III}(OH_2)(PaPy_2Q)]^{2+}$ caused changes in the electronic absorption spectrum consistent with the reformation of the Mn^{III}-hydroxo complex $[Mn^{III}(OH)(PaPy_2Q)]^+$ (Figure 7). In each experiment, the final absorption spectrum after the addition of *p*-cyanopyridine could be fit as a linear combination of the spectra of $[Mn^{III}(OH_2)(PaPy_2Q)]^{2+}$ and $[Mn^{III}(OH)(PaPy_2Q)]^+$, which provided the concentrations of these species at equilibrium. This analysis yielded a pK_a value for $[Mn^{III}(OH_2)(PaPy_2Q)]^{2+}$ of 7.6 ± 0.1 in acetonitrile. This value is very similar to that of $[Mn^{III}(OH_2)(dpaq)]^{2+}$ (pK_a = 6.8),[60] which is expected given the structural similarities of these complexes.

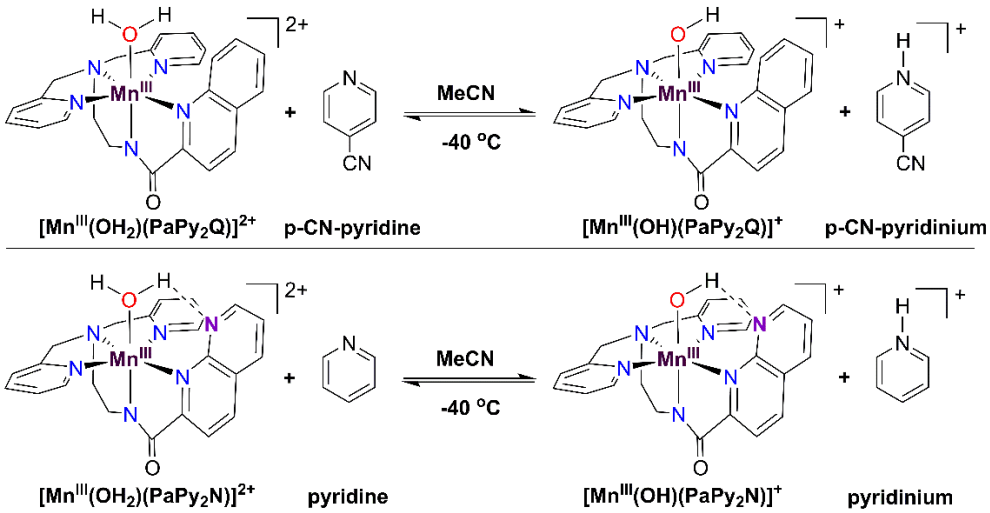

Scheme 2. Reaction of Mn^{III}-aqua complexes with base.

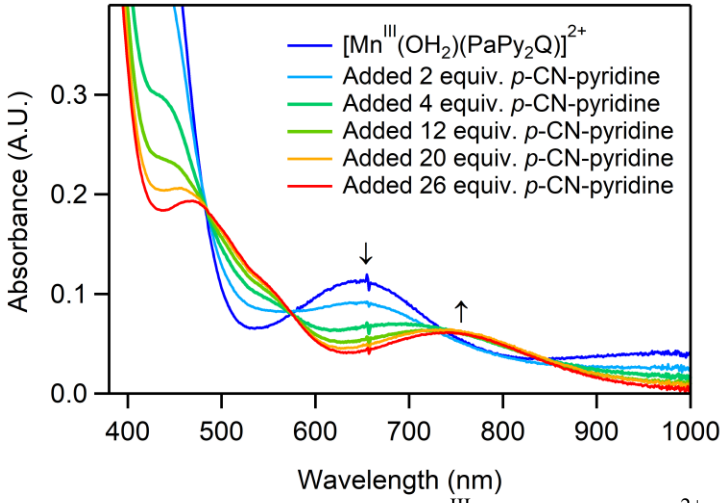

Figure 7. Reaction of 0.5 mM $[Mn^{III}(OH_2)(PaPy_2Q)]^{2+}$ (blue) with increasing concentrations of *p*-cyanopyridine (0 – 13 mM) to generate $[Mn^{III}(OH)(PaPy_2Q)]^{+}$ (red).

When *p*-cyanopyridine was added to $[Mn^{III}(OH_2)(PaPy_2N)]^{2+}$ in MeCN, we observed no reaction, even with as much as 200 equiv. base relative to the Mn^{III}-aqua complex. This lack of reactivity suggests that $[Mn^{III}(OH_2)(PaPy_2N)]^{2+}$ might not be a strong enough acid to react with *p*-cyanopyridine. We therefore explored the reactivity of $[Mn^{III}(OH_2)(PaPy_2N)]^{2+}$ with the stronger base pyridine (pK_a = 12.83 in MeCN).[65] In these reactions, we observed reformation of the Mn^{III}-hydroxo complex (Figure 8), and we were able to fit spectra after the addition of pyridine using linear combinations of spectra from $[Mn^{III}(OH_2)(PaPy_2N)]^{2+}$ and $[Mn^{III}(OH)(PaPy_2N)]^{+}$. These

experiments allowed us to determine a pK_a value of 13.1 ± 0.3 for $[Mn^{III}(OH_2)(PaPy_2N)]^{2+}$. Thus, $[Mn^{III}(OH)(PaPy_2N)]^{+}$ is *ca.* 6 and 7 pK_a units more basic than $[Mn^{III}(OH)(PaPy_2Q)]^{+}$ and $[Mn^{III}(OH)(dpaq)]^{+}$.[60] The enhanced basicity for $[Mn^{III}(OH)(PaPy_2N)]^{+}$ is consistent with previous DFT computations. These calculations predicted pK_a values for the $[Mn^{III}(OH_2)(PaPy_2Q)]^{2+}$ and $[Mn^{III}(OH_2)(PaPy_2N)]^{2+}$ of 6.4 and 13.3, respectively,[49] which are remarkably similar to the experimental values (7.6 ± 0.1 and 13.1 ± 0.3, respectively). We attribute the increased basicity of $[Mn^{III}(OH)(PaPy_2N)]^{+}$ to an intramolecular hydrogen bond enabled by the naphthyridine group.

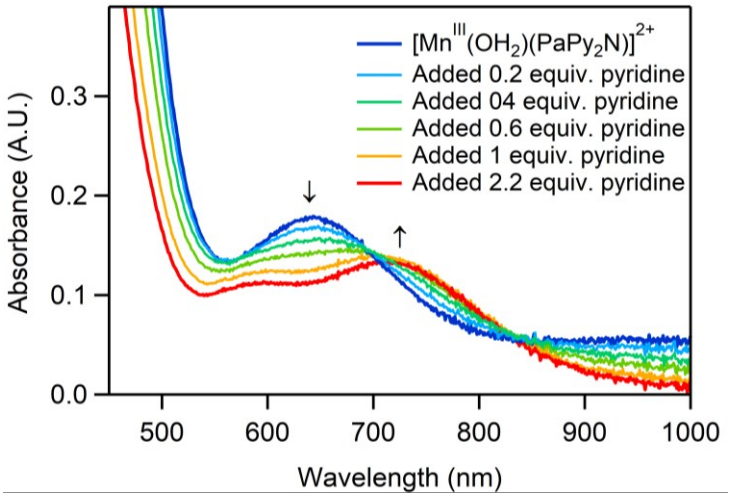

Figure 8. Reaction of 1.25 mM $[Mn^{III}(OH_2)(PaPy_2N)]^{2+}$ (blue) with increasing concentrations of pyridine (0 – 2.75 mM) to generate $[Mn^{III}(OH)(PaPy_2N)]^{+}$ (red).

We determined an estimate of the $Mn^{III/II}$ reduction potentials for $[Mn^{III}(OH_2)(PaPy_2Q)]^{2+}$ and $[Mn^{III}(OH_2)(PaPy_2N)]^{2+}$ by reacting these complexes with one-electron reductants with $E_{1/2}$ values from 0 – 0.67 V vs $Fc^{0/+}$. The addition of ferrocene (0 V vs $Fc^{+/0}$), 1,1′-dibromoferrocene ($E_{1/2}$ = 0.34 V vs $Fc^{+/0}$), 1,1′-diacetylferrocene ($E_{1/2}$ = 0.46 V vs $Fc^{+/0}$), and *p*-bromo-*N*,*N*-dimethylaniline ($E_{1/2}$ = 0.55 V vs $Fc^{+/0}$) to $[Mn^{III}(OH_2)(PaPy_2Q)]^{2+}$ and $[Mn^{III}(OH_2)(PaPy_2N)]^{2+}$ at -40 °C in MeCN resulted in the disappearance of the bands associated with the Mn^{III}-aqua complexes and the formation of bands expected for the oxidized products of the added reductants (Figures S5 – S7). In contrast, no reaction was observed either for $[Mn^{III}(OH_2)(PaPy_2Q)]^{2+}$ or

$[Mn^{III}(OH_2)(PaPy_2N)]^{2+}$ upon the addition of tris(4-bromophenyl)ammoniumyl hexachloroantimonate ($E_{1/2}$ = 0.67 V vs $Fc^{+/0}$). On the basis of these results, we conclude that the reduction potentials for these Mn^{III}-aqua complexes fall between 0.55 and 0.67 V vs $Fc^{+/0}$. These values align well with the potential of 0.63 V vs $Fc^{+/0}$ determined by Nam *et al.* for the $[Mn^{III}(OH_2)(dpaq)]^{2+}$ complex.[60] These potentials are much higher than peak potentials ($E_{p,c}$) observed for the corresponding Mn^{III}-hydroxo complexes $[Mn^{III}(OH)(PaPy_2Q)]^{+}$ or $[Mn^{III}(OH)(PaPy_2N)]^{+}$ (-0.86 and -1.10 V vs $Fc^{+/0}$, respectively), demonstrating the dramatic increase in potential associated with protonation of the hydroxo ligand.[49]

The pK_a values and range of reduction potentials for t allow us to use the Bordwell equation (a modified version of that shown in equation 4) to calculate O–H BDFEs for the Mn^{II}-aqua complexes. For $[Mn^{II}(OH_2)(PaPy_2Q)]^{+}$, we obtain values of 75.7 to 78.6 kcal mol^{-1}, while for $[Mn^{II}(OH_2)(PaPy_2N)]^{+}$ we have higher values of 83.2 to 86.0 kcal mol^{-1}. We thus will use the midpoint values of 77 ± 2 kcal mol^{-1} and 85 ± 2 kcal mol^{-1} for $[Mn^{II}(OH_2)(PaPy_2Q)]^{+}$ and $[Mn^{II}(OH_2)(PaPy_2N)]^{+}$, respectively. These values are remarkably similar to those predicted from DFT computations (78.3 and 84.0 kcal mol^{-1}).[49] The increase in BDFE for $[Mn^{II}(OH_2)(PaPy_2N)]^{+}$ is solely linked to the increase in basicity of the coordinated hydroxo/aqua ligand, which is imparted by the hydrogen-bonding interaction. We can also use the calculated BDFEs and the experimental peak potentials ($E_{p,c}$) for the Mn^{III}-hydroxo complexes to estimate pK_a values for the Mn^{II}-aqua complexes. (This analysis is imperfect, as the peak potentials will not be the same as the reduction potentials.) From this approach, we calculate Mn^{II}-aqua pK_a values of 30 and 40 for $[Mn^{II}(OH_2)(PaPy_2Q)]^{+}$ and $[Mn^{II}(OH_2)(PaPy_2N)]^{+}$, respectively, which are in accordance with DFT predictions (29.6 and 38.2, respectively).[49]

Reactivity of Mn^{III}-hydroxo complexes with acidic phenols. In our previous study of the oxidation of 4-X-2,6-di-*t*-butylphenols (X = Cl, H, ^{t}Bu, Me, and OMe) by these Mn^{III}-hydroxo complexes, the addition of the phenol led to a bleaching of all optical signals of the Mn^{III}-hydroxo complex, which was consistent with the formation of Mn^{II} products.[49] For some phenols, such as 2,4,6-tri-*t*-butyphenol, we observed the formation of bands from the phenoxyl radicals. We also observed a linear correlation between the reaction rate and the phenolic O–H BDFE. On this basis, we concluded that these reactions occurred by a CPET mechanism. However, the phenols considered were not acidic and exhibited a narrow range of pK_a values (~25 – 28). Given the large difference in basicity between the $[Mn^{III}(OH)(PaPy_2Q)]^+$ and $[Mn^{III}(OH)(PaPy_2N)]^+$ complexes, we investigated the reactions of these Mn^{III}-hydroxo complexes with acidic phenols.

The addition of excess 4-nitro-2,6-di-*tert*-butylphenol (4-NO_2-2,6-DTBP) to $[Mn^{III}(OH)(PaPy_2Q)]^+$ in MeCN at 50 °C led to the disappearance of the electronic absorption bands of the Mn^{III}-hydroxo unit and the growth of absorption intensity at wavelengths less than 510 nm (Figure 9, top). This reaction followed first-order kinetics (Figure 9, top inset), and an analysis of the reaction at various substrate concentrations yielded a k_2 value of 0.039 $M^{-1}s^{-1}$ (Figure S9). This rate is *faster* than that observed for the oxidation of 4-H-2,6-DTBP and 4-Cl-2,6-DTBP by $[Mn^{III}(OH)(PaPy_2Q)]^+$ (0.012 and 0.0323 $M^{-1}s^{-1}$, respectively).[49] The increased rate for 4-NO_2-2,6-DTBP is surprising given that the O–H BDFE for this substrate is ~4 kcal mol^{-1} *higher* than those of 4-H-2,6-DTBP and 4-Cl-2,6-DTBP.[42] While we do not observe any transient intermediates in this reaction, the $[Mn^{III}(OH_2)(PaPy_2Q)]^{2+}$ complex, which would be the product of a proton-transfer reaction, has low thermal stability and was characterized at -40 °C (Figure 3). Thus, we presume that, if formed, we would not observe the accumulation of $[Mn^{III}(OH_2)(PaPy_2Q)]^{2+}$ due to its instability at 50 °C.

The $[Mn^{III}(OH)(PaPy_2N)]^+$ complex also shows a reaction with 4-NO_2-2,6-DTBP at 50 °C in MeCN (Figure 9, bottom). In this case, when the optical signals of the Mn^{III}-hydroxo complex bleach, we observe the growth and decay of signals near 550 and 1050 nm. During the decay, there is also a subtle shift of the absorption maximum at ~730 nm to ~650 nm (Figure 9, bottom, green trace). We attribute these spectral changes to the transient formation of the Mn^{III}-aqua complex $[Mn^{III}(OH_2)(PaPy_2N)]^{2+}$. This complex is unstable at 50 °C and decays with time. Despite the complexity of the decay process, the absorption decay of $[Mn^{III}(OH_2)(PaPy_2N)]^{2+}$ at 800 nm can be fit to a first-order process, and we determined a k_2 for this reaction of 0.3 $M^{-1}s^{-1}$ at 50 °C (Figure S9). This rate is only slightly less than that observed for the reaction of $[Mn^{III}(OH)(PaPy_2N)]^+$ with 4-H-DTBP (0.99 M^{-1} s^{-1}) despite the ~4 kcal mol^{-1} increase in O–H BDFE from 4-NO_2-2,6-DTBP to 4-H-2,6-DTBP.

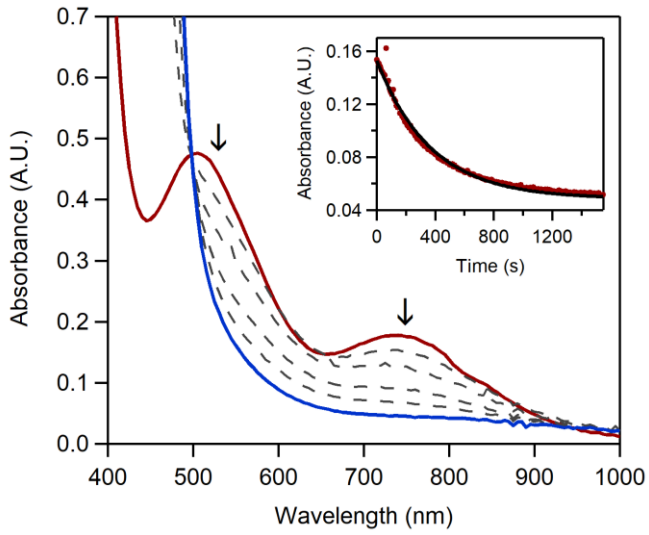

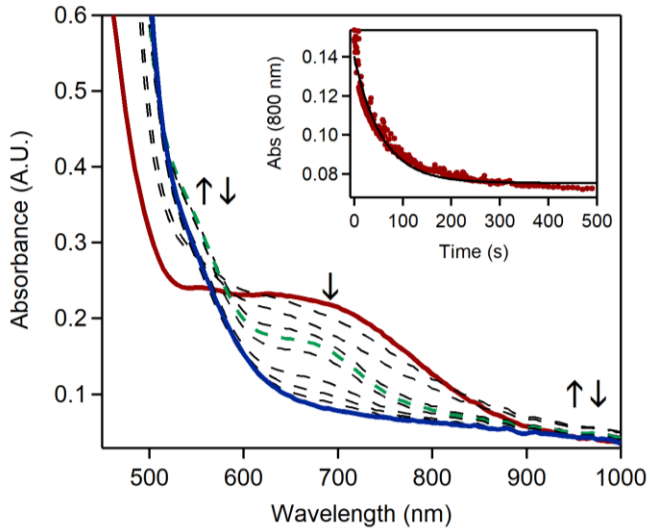

Figure 9. Electronic absorption spectrum showing the decay of $[Mn^{III}(OH)(PaPy_2Q)]^+$ (top) and $[Mn^{III}(OH)(PaPy_2N)]^+$ (bottom) in the presence of an excess of 4-NO_2-DTBP in MeCN at 50 °C. The starting spectra are red and the final spectra are blue. For the reaction of $[Mn^{III}(OH)(PaPy_2N)]^+$, a green trace marks an intermediate that is attributed to the accumulation of $[Mn^{III}(OH_2)(PaPy_2N)]^+$. In each plot, the inset shows the decay of the Mn^{III}-hydroxo complex in the presence of 50 equiv. 4-NO_2-DTBP in MeCN at 50 °C.

Thermodynamic Analysis of Phenol Oxidation by Mn^{III}-hydroxo Complexes. In this section, we use our experimental thermodynamic data for $[Mn^{II}(OH_2)(PaPy_2Q)]^+$ and $[Mn^{II}(OH_2)(PaPy_2N)]^+$ with corresponding parameters for phenol substrates to evaluate trends in reactivity. This analysis requires accurate values for the BDFEs, pK_a, and $E_{1/2}$ of the phenols. Because these data are not available for all phenols in MeCN, we used DFT methods to calculate these values. We describe this approach and its validation in the Supplementary Information. We also discuss a complementary approach in the Supplementary Information, where we calculate reaction free energies solely using DFT computations. This procedure follows that used by Anderson and co-workers in a recent investigation of phenol oxidation by Co^{III}-oxo complexes.[42] As discussed in the Supplementary Information, the trends for the DFT-only approach are the same as those when using the experimental thermodynamic parameters for the Mn^{III}-hydroxo complexes. The only difference is in the absolute values of the reaction free energies.

When we consider phenol oxidation by $[Mn^{III}(OH)(PaPy_2Q)]^+$ and $[Mn^{III}(OH)(PaPy_2N)]^+$ and, for the moment, exclude the results for 4-NO_2-DTBP, we observe an excellent linear correlation (R^2 = 0.96) between the reaction barrier (as ln(k_2)RT) versus the free energy for proton-electron transfer (ΔG_{CPET}; see Figure 10, left). All reactions are either exoergic or only slightly endoergic ($\Delta G_{CPET} \leq 0$). The data points for reactions with $[Mn^{III}(OH)(PaPy_2Q)]^+$ and $[Mn^{III}(OH)(PaPy_2N)]^+$ nearly fall on the same fit lines, and the linear fit in each case yields slopes near -0.5, which is typical of a Bell-Evans-Polanyi relationship.[66] The data points for the reactions with 4-NO_2-2,6-DTBP are notable outliers. For example, ΔG_{CPET} for a reaction between $[Mn^{III}(OH)(PaPy_2N)]^+$ and 4-NO_2-DTBP is -0.6 kcal mol^{-1}. From the trend line in Figure 10 (left), we expect the rate of reaction between $[Mn^{III}(OH)(PaPy_2N)]^+$ and 4-NO_2-DTBP to be 0.02 $M^{-1}s^{-1}$, which is more than an order of magnitude smaller than the experimental rate (0.33 $M^{-1}s^{-1}$). The experimental rate for $[Mn^{III}(OH)(PaPy_2Q)]^+$ is even more of an outlier (Figure 10, left). In this case, ΔG_{CPET} = 7.4 kcal mol^{-1}, and the trend line predicts an experimental rate of 1×10^{-4} $M^{-1}s^{-1}$, which is approximately 400-fold slower than the experimental rate of 0.039 $M^{-1}s^{-1}$. This lack of conformity to the established trend for CPET reactions suggests a change in reaction mechanism caused by the increased acidity of the 4-NO_2-DTBP substrate. We propose that these reactions proceed by a proton-transfer mechanism, which is supported by the appearance of $[Mn^{III}(OH_2)(PaPy_2N)]^{2+}$ for the reaction of $[Mn^{III}(OH)(PaPy_2N)]^+$ with 4-NO_2-DTBP (Figure 9, bottom).

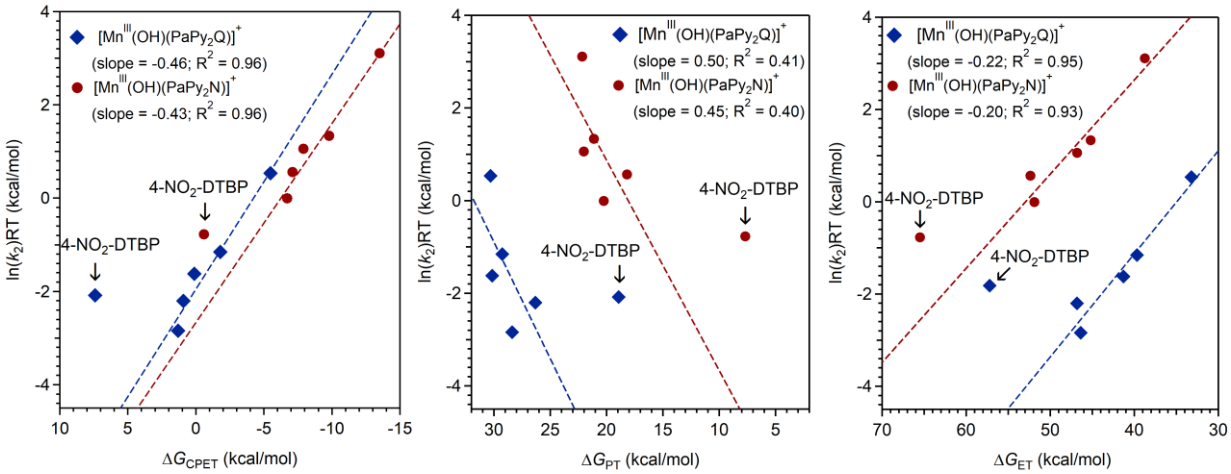

Figure 10. Correlation of the reaction rates of phenol oxidation by $[Mn^{III}(OH)(PaPy_2Q)]^+$ and $[Mn^{III}(OH)(PaPy_2N)]^+$ with the overall proton-electron transfer driving force (left), the driving force for initial proton transfer (center), and the driving force for initial electron transfer. The blue circles are data points for $[Mn^{III}(OH)(PaPy_2Q)]^+$ and the red diamonds are data points for $[Mn^{III}(OH)(PaPy_2N)]^+$. The linear fit lines exclude the data points for reactions with 4-NO_2-DTBP. In these plots, all reaction free energies were determined using experimental values for the metal complexes and DFT-calculated values for the phenols.

We also plotted the experimental reaction rates versus ΔG_{PT} and ΔG_{ET} (see Figure 10, center and right). The proton-transfer reactions are all endoergic (ΔG_{PT} > 15 kcal mol^{-1}). While the plot of rate versus ΔG_{PT} for all phenols except 4-NO_2-DTBP shows poor linearity ($R^2 < 0.5$), there is a trend of slower reaction rates as the proton-transfer driving force becomes *more favorable* (*i.e.*, ΔG_{PT} becomes a smaller, positive number). This general trend, along with the overall positive values for ΔG_{PT}, presents a strong case against a mechanism involving initial proton transfer. The data points for reactions with 4-NO_2-DTBP are clear outliers and are the only points that show a trend of increased rate with more favorable (*i.e.*, less positive) ΔG_{PT}.

A plot of experimental reaction rates versus ΔG_{ET} for all phenols but 4-NO_2-DTBP is very linear ($R^2 \approx 0.92$), illustrating an increase in rate with a more favorable electron-transfer driving force. The small slope (-0.20) shows that the rate is less sensitive to the electron-transfer driving force than to the proton-transfer driving force (slope ≈ 0.50). The ΔG_{ET} is a large, positive value

for each reaction (> 30 kcal mol^{-1}), illustrating that an initial electron-transfer reaction is unfavorable. We note that in these plots, the reactions of the Mn^{III}-hydroxo complexes with the 4-NO_2-DTPB remain marked outliers, with rates several orders of magnitude faster than expected based on the trend lines.

One potential caveat to our conclusion that the reactions of the Mn^{III}-hydroxo complexes with 4-NO_2-DTBP proceed by a PT reaction is that ΔG_{PT} is positive for these reactions (~7 to 18 kcal mol^{-1}; see Figure 10). However, we note that there are likely systematic errors in our calculated thermodynamic parameters for the phenols. As discussed in the Supplementary Information, an alternative approach to determining thermodynamic parameters that used a different density functional revealed the same trends as shown in the main text, but with different absolute values for ΔG_{CPET}, ΔG_{PT}, and ΔG_{ET} (see Figure S10). In that case, ΔG_{CPET} and ΔG_{PT} for reactions of the Mn^{III}-hydroxo complexes with 4-NO_2-DTBP are nearly identical (~16 kcal mol^{-1} for $[Mn^{III}(OH)(PaPy_2Q)]^+$ and ~9 kcal mol^{-1} for $[Mn^{III}(OH)(PaPy_2Q)]^+$; see Tables S5 and S6), in better agreement with the mechanistic crossover.

Finally, we examine the dependence of the rate in terms of the asynchronicity (equation 1).[33] (We also examined the reactions in terms of frustration, $\Delta G_{PT} + \Delta G_{ET}$, and $\Delta G^{\neq}_{thermo}$ (equations 2 – 3).[37] While there is a correlation with the reaction barrier with $\Delta G_{PT} + \Delta G_{ET}$, the analysis in terms of frustration and $\Delta G^{\neq}_{thermo}$ had limited success, potentially due to sensitivities in frustration to errors in the thermodynamic parameters. We describe these results in the Supporting Information.) We first examine asynchronicity using both η and $\Delta G_{PT} - \Delta G_{ET}$ (equation 1). (We note that η and $\Delta G_{PT} - \Delta G_{ET}$ are related by a prefactor of $1/\sqrt{2}$; see equation 1. Our plot here uses $\Delta G_{PT} - \Delta G_{ET}$ to permit a later comparison with a recent study by Mayer and co-workers.[66])

When considering all phenols but 4-NO_2-DTBP, the plot of reaction rate versus ΔG_{PT} - ΔG_{ET} is very linear ($R^2 \approx 0.9$), with slopes of ~0.16 (Figure 11, left). First, we note that the ΔG_{PT} - ΔG_{ET} term is negative in all cases, which reflects a more favorable driving force for PT over ET. Consequently, all these reactions show PT-favored asynchronicity. However, as seen from Figure 10, the change in driving force among the series of phenol oxidation reactions primarily comes from changes in the ΔG_{ET} term. Thus, this series displays PT-favored but ET-varied asynchronicity. Second, these plots show an increase in rate as the difference between ΔG_{PT} and ΔG_{ET} *decreases*. Indeed, the reaction of 4-MeO-DTBP with $[Mn^{III}(OH)(PaPy_2Q)]^+$ is the fastest for this series, and this reaction has nearly equal and oppositely signed ΔG_{PT} and ΔG_{ET} terms (*i.e.*, ΔG_{PT} - $\Delta G_{ET} \approx 0$). We also include a plot of the reaction barriers versus $-|\eta|/4$, as this term is included in the expression for the barrier (equation 1). The plot of $\ln(k_2)RT$ versus $-|\eta|/4$ is linear, with a slope near 1 (Figure 11, right), indicating that the change in the barrier is of the order of that predicted by equation 3, but the slope has the wrong sign. Thus, for these reactions of Mn^{III}-hydroxo complexes with phenols, an increase in the reaction asynchronicity (ΔG_{PT} - ΔG_{ET}) does not correlate with a faster reaction rate. In fact, we observe the opposite trend. A potential exception are the reactions with 4-NO_2-2,6-DTBP. These reactions are the most asynchronous of the series and are anomalously fast. However, in these cases, we attribute the anomalously fast rates to a change in mechanism from CPET to proton transfer.

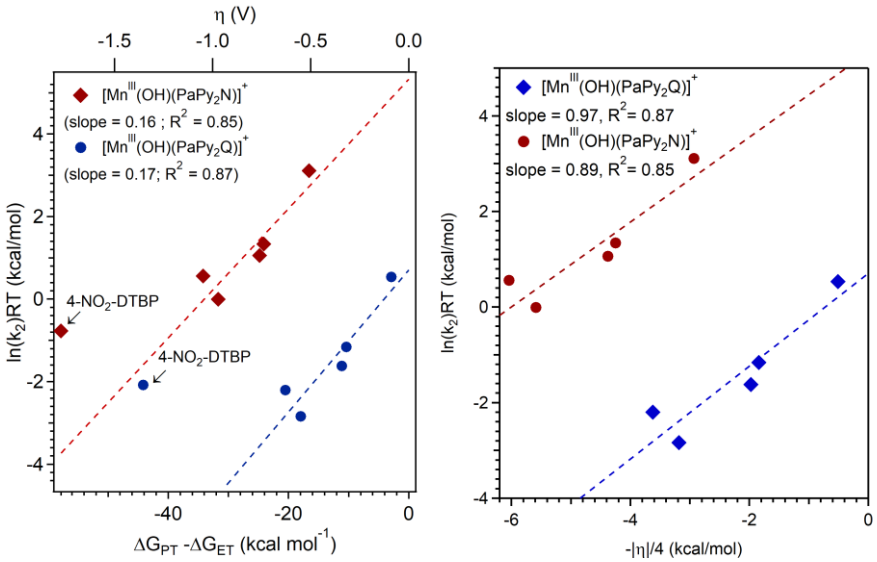

Figure 11. Correlation of the reaction rates of phenol oxidation by $[Mn^{III}(OH)(PaPy_2Q)]^+$ and $[Mn^{III}(OH)(PaPy_2N)]^+$ with the difference in proton-transfer and electron-transfer driving force (left; bottom axis) and asynchronicity (left; top axis) and with $-|\eta|/4$ (right). The blue circles are data points for $[Mn^{III}(OH)(PaPy_2Q)]^+$ and the red diamonds are data points for $[Mn^{III}(OH)(PaPy_2N)]^+$. The linear fit lines exclude the data points for reactions with 4-NO_2-DTBP, and the data for this substrate are excluded from the graph on the right. In these plots, all reaction free energies were determined using experimental values for the metal complexes and DFT-calculated values for the phenols.

Conclusions.

Manganese catalysts are used in both synthetic and biological systems to perform a variety of oxidation-reduction reactions.[19, 21, 25, 67] In many of these examples, a key step in the catalytic cycle involves a manganese-oxygen species accepting a proton and an electron from a substrate molecule. More generally, PCET reactions are ubiquitous in biological and synthetic catalysis,[27-32] and a major goal in this field is to classify and identify factors that control PCET reactions.

While the past several years have seen important advances in our understanding of CPET reactions, a basic requirement for most analyses is knowledge of thermodynamic data (*i.e.*, BDFEs, pK_a values, and reduction potentials) for metal-oxygen intermediates. In this work, we generated a pair of Mn^{III}-aqua complexes by reacting Mn^{III}-hydroxo species with strong acids and used a variety of spectroscopic and computational methods to characterize these complexes. A

comparison of experimental and TD-DFT electronic absorption spectra provide strong support that the hydroxo is the site of protonation. Titration experiments yielded pK_a values for the Mn^{III}-aqua complexes. The putative hydrogen bond in $[Mn^{III}(OH)(PaPy_2N)]^+$ increases the basicity of the hydroxo ligand by over 5 pH units, which leads to an increase in the O-H BDFE of the Mn^{II}-aqua complex of ~8 kcal mol^{-1}. Notably, prior studies of Mn^{III}-OH complexes that relied on changes in the ligand sphere lead to only modest net changes in O–H BDFE due to offsetting changes in metal reduction potential and basicity.[45] The new experimental data allowed us to evaluate CPET reaction rates according to thermodynamic models of reactivity.

In the broad literature on PCET reactions, there are growing examples where ΔG_{CPET} appears to be insufficient in explaining trends in reactivity. For example, in hydrocarbon oxidation by Co^{III}-oxo complexes, better correlations exist between reaction barriers and substrate acidity.[35] In other cases, better agreement with experimental rate trends is achieved by augmenting the ΔG_{CPET} term with changes in the proton-transfer or electron-transfer driving force (ΔG_{PT} and ΔG_{ET}).[38, 68] However, using the newly determined thermodynamic parameters for the Mn^{III}-hydroxo complexes explored in this present study, we observe that the reaction barriers for phenol oxidation (expressed as ln(k_2)RT) show a strong linear correlation with ΔG_{CPET} (Figure 10, left). Thus, the rate variations are well described by changes in ΔG_{CPET}. Nonetheless, a plot of reaction rates versus ΔG_{PT} - ΔG_{ET} does reveal a linear correlation. In a recent study of the oxidation of substituted toluenes by ^{t}Bu•, ^{t}BuO•, and ^{t}BuOO•, Mayer and co-workers observed that plots of reaction barrier versus ΔG_{PT} - ΔG_{ET} were linear, but with very small slopes of -0.02 to -0.03.[66] In this present study, we observe larger slopes of ~0.16 (Figure 11). According to the formulation of asynchronicity, the barrier is sensitive to -|η|/4 (equation 3),[33] and our observed slopes are close to this prediction (see Figure 11, right). The reason for the different slopes for organic radicals and these Mn^{III}-hydroxo

complexes is unclear at present. Moreover, the rates of phenol oxidation by the Mn^{III}-hydroxo complexes increase with less asynchronous reactions. This observation runs counter to other cases, where faster rates were attributed to more asynchronous, or imbalanced, proton-electron transfer.[34-35, 38-40] However, faster rates are only predicted for asynchronous reactions when this term is a dominant contributor to the free energy barrier or correlates proportionally with another dominant factor.[69] Although we were unable to perform a meaningful analysis of the contribution of frustration to the barrier (see the Supplementary Information), our preliminary data suggest that the asynchronicity might be offset by frustration, such that these off-diagonal contributions are roughly constant and ΔG_{CPET} becomes the best predictor of reactivity.

Our observed trends between reaction rates and driving force fail for reactions involving the more acidic 4-NO_2-DTBP substrate (Figure 11). For this substrate, we observe reaction rates that are 10- to 400-fold faster than that expected based on the linear free energy relationship established by reactions with other phenols. Such a clear deviation implies a change in mechanism. This conclusion is bolstered by the observation of a transient intermediate in the reaction of 4-NO_2-DTBP with $[Mn^{III}(OH)(PaPy_2N)]^+$ that resembles the Mn^{III}-aqua complex (Figure 9, bottom). Thus, in this work, we can use both the thermodynamic and kinetic trends and the observation of an intermediate to support a mechanistic crossover. This study reveals the continued power of measured thermodynamic parameters in understanding the intricacies of reactions involving proton and electron transfer.

Supporting Information. Electronic absorption spectra, NMR data, discussion of variable-temperature NMR data, kinetic data, discussion of thermodynamic analysis of phenol oxidation reactions, including data tables and figures, and Cartesian coordinates from DFT computations (PDF).

Acknowledgements. This work was supported by the U.S. National Science Foundation (CHE-2154955 to T. A. J.), by the National Institutes of Health Graduate Training at the Biology-Chemistry Interface Grant (5T32GM132061-05 to M. J. A. L.) from the National Institutes of General Medical Sciences, and the Grant Agency of the Czech Republic (Grant No. 24-11247S to M.S.). The calculations were performed at the University of Kansas Center for Research Computing (CRC), including the BigJay Cluster resource funded through U.S. NSF Grant MRI-2117449.

Data availability. The data supporting this article have been included as part of the Supplementary Information.

Author contributions. P. S., M. J. A. L., A. A. O., and T. A. J. conceived and planned the experiments. P. S., M. J. A. L., A. A. O., and B. B. N. performed all experiments and computations. All authors contributed to data analysis and provided contributions to writing of the final manuscript.

References.

1. Ray, K.; Pfaff, F. F.; Wang, B.; Nam, W., Status of reactive non-heme metal-oxygen intermediates in chemical and enzymatic reactions. *J. Am. Chem. Soc.* **2014,** *136* (40), 13942-13958.
2. Neu, H. M.; Baglia, R. A.; Goldberg, D. P., A Balancing Act: Stability versus Reactivity of Mn(O) Complexes. *Acc. Chem. Res.* **2015,** *48* (10), 2754-2764.
3. Yano, J.; Yachandra, V., Mn4Ca Cluster in Photosynthesis: Where and How Water is Oxidized to Dioxygen. *Chem. Rev.* **2014,** *114* (8), 4175-4205.
4. Cook, E. N.; Machan, C. W., Homogeneous catalysis of dioxygen reduction by molecular Mn complexes. *Chem. Commun.* **2022,** *58* (84), 11746-11761.
5. Cook, E. N.; Machan, C. W., Bioinspired mononuclear Mn complexes for O2 activation and biologically relevant reactions. *Dalton Trans.* **2021,** *50* (46), 16871-16886.
6. Rice, D. B.; Massie, A. A.; Jackson, T. A., Manganese–Oxygen Intermediates in O–O Bond Activation and Hydrogen-Atom Transfer Reactions. *Acc. Chem. Res.* **2017,** *50* (11), 2706-2717.
7. Mayfield, J. R.; Grotemeyer, E. N.; Jackson, T. A., Concerted proton–electron transfer reactions of manganese–hydroxo and manganese–oxo complexes. *Chem. Commun.* **2020,** *56* (65), 9238-9255.

8. Zhu, W.; Richards, N. G. J., Biological functions controlled by manganese redox changes in mononuclear Mn-dependent enzymes. *Essays In Biochemistry* **2017,** *61* (2), 259-270.
9. Kovacs, J. A., Tuning the Relative Stability and Reactivity of Manganese Dioxygen and Peroxo Intermediates via Systematic Ligand Modification. *Acc. Chem. Res.* **2015,** *48* (10), 2744-2753.
10. Sheng, Y.; Abreu, I. A.; Cabelli, D. E.; Maroney, M. J.; Miller, A.-F.; Teixeira, M.; Valentine, J. S., Superoxide Dismutases and Superoxide Reductases. *Chem. Rev.* **2014,** *114* (7), 3854-3918.
11. Kostenko, A.; Ray, K.; Iavarone, A. T.; Offenbacher, A. R., Kinetic Characterization of the C–H Activation Step for the Lipoxygenase from the Pathogenic Fungus Magnaporthe oryzae: Impact of N-Linked Glycosylation. *Biochemistry* **2019,** *58* (29), 3193-3203.
12. Wennman, A.; Oliw, E. H.; Karkehabadi, S.; Chen, Y., Crystal Structure of Manganese Lipoxygenase of the Rice Blast Fungus Magnaporthe oryzae. *J. Biol. Chem.* **2016,** *291*, 8130-8139.
13. Wennman, A.; Karkehabadi, S.; Oliw, E. H., Kinetic investigation of the rate-limiting step of manganese- and iron-lipoxygenases. *Arch. Biochem. Biophys.* **2014,** *555–556* (0), 9-15.
14. Rose, H. R.; Ghosh, M. K.; Maggiolo, A. O.; Pollock, C. J.; Blaesi, E. J.; Hajj, V.; Wei, Y.; Rajakovich, L. J.; Chang, W.-c.; Han, Y.; Hajj, M.; Krebs, C.; Silakov, A.; Pandelia, M.-E.; Bollinger, J. M.; Boal, A. K., Structural Basis for Superoxide Activation of Flavobacterium johnsoniae Class I Ribonucleotide Reductase and for Radical Initiation by Its Dimanganese Cofactor. *Biochemistry* **2018,** *57* (18), 2679-2693.
15. Cotruvo, J. A.; Stich, T. A.; Britt, R. D.; Stubbe, J., Mechanism of Assembly of the Dimanganese-Tyrosyl Radical Cofactor of Class Ib Ribonucleotide Reductase: Enzymatic Generation of Superoxide Is Required for Tyrosine Oxidation via a Mn(III)Mn(IV) Intermediate. *J. Am. Chem. Soc.* **2013,** *135* (10), 4027-4039.
16. Nandy, A.; Adamji, H.; Kastner, D. W.; Vennelakanti, V.; Nazemi, A.; Liu, M.; Kulik, H. J., Using Computational Chemistry To Reveal Nature's Blueprints for Single-Site Catalysis of C–H Activation. *ACS Catal.* **2022,** *12* (15), 9281-9306.
17. Philip, R. M.; Radhika, S.; Abdulla, C. M. A.; Anilkumar, G., Recent Trends and Prospects in Homogeneous Manganese-Catalysed Epoxidation. *Adv. Synth. Catal.* **2021,** *363* (5), 1272-1289.
18. Guo, M.; Lee, Y.-M.; Fukuzumi, S.; Nam, W., Biomimetic metal-oxidant adducts as active oxidants in oxidation reactions. *Coord. Chem. Rev.* **2021,** *435*, 213807.
19. Vicens, L.; Olivo, G.; Costas, M., Rational Design of Bioinspired Catalysts for Selective Oxidations. *ACS Catal.* **2020,** *10* (15), 8611-8631.
20. Chen, J.; Jiang, Z.; Fukuzumi, S.; Nam, W.; Wang, B., Artificial nonheme iron and manganese oxygenases for enantioselective olefin epoxidation and alkane hydroxylation reactions. *Coord. Chem. Rev.* **2020,** *421*, 213443.
21. Sun, W.; Sun, Q., Bioinspired Manganese and Iron Complexes for Enantioselective Oxidation Reactions: Ligand Design, Catalytic Activity, and Beyond. *Acc. Chem. Res.* **2019,** *52* (8), 2370-2381.
22. Guo, M.; Corona, T.; Ray, K.; Nam, W., Heme and Nonheme High-Valent Iron and Manganese Oxo Cores in Biological and Abiological Oxidation Reactions. *ACS Cent. Sci.* **2019,** *5* (1), 13-28.
23. Ottenbacher, R. V.; Talsi, E. P.; Bryliakov, K. P., Chiral Manganese Aminopyridine Complexes: the Versatile Catalysts of Chemo- and Stereoselective Oxidations with H2O2. *Chem. Rec.* **2018,** *18* (1), 78-90.
24. Chambers, R. K.; Weaver, J. D.; Kim, J.; Hoar, J. L.; Krska, S. W.; White, M. C., A preparative small-molecule mimic of liver CYP450 enzymes in the aliphatic C-H oxidation of carbocyclic N heterocycles. *Proc. Natl. Acad. Sci. U.S.A.* **2023,** *120* (29), e2300315120.
25. Call, A.; Capocasa, G.; Palone, A.; Vicens, L.; Aparicio, E.; Choukairi Afailal, N.; Siakavaras, N.; López Saló, M. E.; Bietti, M.; Costas, M., Highly Enantioselective Catalytic Lactonization at Nonactivated Primary and Secondary γ-C–H Bonds. *J. Am. Chem. Soc.* **2023,** *145* (32), 18094-18103.
26. Offenbacher, A. R.; Holman, T. R., Fatty Acid Allosteric Regulation of C-H Activation in Plant and Animal Lipoxygenases. *Molecules* **2020,** *25* (15), 3374.

27. Agarwal, R. G.; Coste, S. C.; Groff, B. D.; Heuer, A. M.; Noh, H.; Parada, G. A.; Wise, C. F.; Nichols, E. M.; Warren, J. J.; Mayer, J. M., Free Energies of Proton-Coupled Electron Transfer Reagents and Their Applications. *Chem. Rev.* **2022,** *122* (1), 1-49.
28. Darcy, J. W.; Koronkiewicz, B.; Parada, G. A.; Mayer, J. M., A Continuum of Proton-Coupled Electron Transfer Reactivity. *Acc. Chem. Res.* **2018,** *51* (10), 2391-2399.
29. Tyburski, R.; Liu, T.; Glover, S. D.; Hammarström, L., Proton-Coupled Electron Transfer Guidelines, Fair and Square. *J. Am. Chem. Soc.* **2021,** *143* (2), 560-576.
30. Liu, T.; Tyburski, R.; Wang, S.; Fernández-Terán, R.; Ott, S.; Hammarström, L., Elucidating Proton-Coupled Electron Transfer Mechanisms of Metal Hydrides with Free Energy- and Pressure-Dependent Kinetics. *J. Am. Chem. Soc.* **2019,** *141* (43), 17245-17259.
31. Solis, B. H.; Hammes-Schiffer, S., Proton-Coupled Electron Transfer in Molecular Electrocatalysis: Theoretical Methods and Design Principles. *Inorg. Chem.* **2014,** *53* (13), 6427-6443.
32. Hammes-Schiffer, S., Introduction: Proton-Coupled Electron Transfer. *Chem. Rev.* **2010,** *110* (12), 6937-6938.
33. Bím, D.; Maldonado-Domínguez, M.; Rulíšek, L.; Srnec, M., Beyond the classical thermodynamic contributions to hydrogen atom abstraction reactivity. *Proc. Natl. Acad. Sci. U.S.A.* **2018,** *115* (44), E10287-E10294.
34. Mandal, M.; Elwell, C. E.; Bouchey, C. J.; Zerk, T. J.; Tolman, W. B.; Cramer, C. J., Mechanisms for Hydrogen-Atom Abstraction by Mononuclear Copper(III) Cores: Hydrogen-Atom Transfer or Concerted Proton-Coupled Electron Transfer? *J. Am. Chem. Soc.* **2019,** *141* (43), 17236-17244.
35. Goetz, M. K.; Anderson, J. S., Experimental Evidence for pKa-Driven Asynchronicity in C–H Activation by a Terminal Co(III)–Oxo Complex. *J. Am. Chem. Soc.* **2019,** *141* (9), 4051-4062.
36. Usharani, D.; Lacy, D. C.; Borovik, A. S.; Shaik, S., Dichotomous Hydrogen Atom Transfer vs Proton-Coupled Electron Transfer During Activation of X–H Bonds (X = C, N, O) by Nonheme Iron–Oxo Complexes of Variable Basicity. *J. Am. Chem. Soc.* **2013,** *135* (45), 17090-17104.
37. Maldonado-Domínguez, M.; Srnec, M., H-Atom Abstraction Reactivity through the Lens of Asynchronicity and Frustration with Their Counteracting Effects on Barriers. *Inorg. Chem.* **2022,** *61* (47), 18811-18822.
38. Barman, S. K.; Yang, M.-Y.; Parsell, T. H.; Green, M. T.; Borovik, A. S., Semiempirical method for examining asynchronicity in metal–oxido-mediated C–H bond activation. *Proc. Natl. Acad. Sci. U.S.A.* **2021,** *118* (36), e2108648118.
39. Kotani, H.; Shimomura, H.; Ikeda, K.; Ishizuka, T.; Shiota, Y.; Yoshizawa, K.; Kojima, T., Mechanistic Insight into Concerted Proton–Electron Transfer of a Ru(IV)-Oxo Complex: A Possible Oxidative Asynchronicity. *J. Am. Chem. Soc.* **2020,** *142* (40), 16982-16989.
40. Coste, S. C.; Brezny, A. C.; Koronkiewicz, B.; Mayer, J. M., C–H oxidation in fluorenyl benzoates does not proceed through a stepwise pathway: revisiting asynchronous proton-coupled electron transfer. *Chem. Sci.* **2021,** *12* (39), 13127-13136.
41. Dhar, D.; Yee, G. M.; Markle, T. F.; Mayer, J. M.; Tolman, W. B., Reactivity of the copper(iii)-hydroxide unit with phenols. *Chem. Sci.* **2017,** *8* (2), 1075-1085.
42. Zhao, N.; Goetz, M. K.; Schneider, J. E.; Anderson, J. S., Testing the Limits of Imbalanced CPET Reactivity: Mechanistic Crossover in H-Atom Abstraction by Co(III)–Oxo Complexes. *J. Am. Chem. Soc.* **2023,** *145* (10), 5664-5673.
43. Goldsmith, C. R.; Cole, A. P.; Stack, T. D. P., C−H Activation by a Mononuclear Manganese(III) Hydroxide Complex: Synthesis and Characterization of a Manganese-Lipoxygenase Mimic? *J. Am. Chem. Soc.* **2005,** *127* (27), 9904-9912.
44. Coggins, M. K.; Brines, L. M.; Kovacs, J. A., Synthesis and Structural Characterization of a Series of MnIIIOR Complexes, Including a Water-Soluble MnIIIOH That Promotes Aerobic Hydrogen-Atom Transfer. *Inorg. Chem.* **2013,** *52* (21), 12383-12393.
45. Rice, D. B.; Munasinghe, A.; Grotemeyer, E. N.; Burr, A. D.; Day, V. W.; Jackson, T. A., Structure and Reactivity of (μ-Oxo)dimanganese(III,III) and Mononuclear Hydroxomanganese(III) Adducts

Supported by Derivatives of an Amide-Containing Pentadentate Ligand. *Inorg. Chem.* **2019,** *58* (1), 622-636.
46. Rice, D. B.; Wijeratne, G. B.; Burr, A. D.; Parham, J. D.; Day, V. W.; Jackson, T. A., Steric and Electronic Influence on Proton-Coupled Electron-Transfer Reactivity of a Mononuclear Mn(III)-Hydroxo Complex. *Inorg. Chem.* **2016,** *55* (16), 8110-8120.
47. Wijeratne, G. B.; Corzine, B.; Day, V. W.; Jackson, T. A., Saturation Kinetics in Phenolic O–H Bond Oxidation by a Mononuclear Mn(III)–OH Complex Derived from Dioxygen. *Inorg. Chem.* **2014,** *53* (14), 7622-7634.
48. Opalade, A. A.; Grotemeyer, E. N.; Jackson, T. A., Mimicking Elementary Reactions of Manganese Lipoxygenase Using Mn-hydroxo and Mn-alkylperoxo Complexes. *Molecules* **2021,** *26* (23), 7151.
49. Opalade, A. A.; Hessefort, L.; Day, V. W.; Jackson, T. A., Controlling the Reactivity of a Metal-Hydroxo Adduct with a Hydrogen Bond. *J. Am. Chem. Soc.* **2021,** *143* (37), 15159–15175.
50. Eroy-Reveles, A. A.; Leung, Y.; Beavers, C. M.; Olmstead, M. M.; Mascharak, P. K., Near-Infrared Light Activated Release of Nitric Oxide from Designed Photoactive Manganese Nitrosyls: Strategy, Design, and Potential as NO Donors. *J. Am. Chem. Soc.* **2008,** *130* (13), 4447-4458.
51. Favier, I.; Duñach, E., New protic salts of aprotic polar solvents. *Tet. Lett.* **2004,** *45* (17), 3393-3395.
52. Neese, F., The ORCA program system. *Wiley Interdiscip. Rev. Comput. Mol. Sci.* **2012,** *2* (1), 73-78.
53. Neese, F., Software update: The ORCA program system—Version 5.0. *Wiley Interdiscip. Rev. Comput. Mol. Sci.* **2022,** *12* (5), e1606.
54. Lee, C.; Yang, W.; Parr, R. G., Development of the Colle-Salvetti Correlation-energy Formula into a Functional of the Electron Density. *Phys. Rev. B* **1988,** *37* (2), 785-789.
55. Becke, A. D., Density-functional Thermochemistry. III. The Role of Exact Exchange. *J. Chem. Phys.* **1993,** *98* (7), 5648-5652.
56. Weigend, F., Accurate Coulomb-fitting basis sets for H to Rn. *PCCP* **2006,** *8* (9), 1057-1065.
57. Weigend, F.; Ahlrichs, R., Balanced basis sets of split valence, triple zeta valence and quadruple zeta valence quality for H to Rn: Design and assessment of accuracy. *PCCP* **2005,** *7* (18), 3297-3305.
58. Izsák, R.; Neese, F., An overlap fitted chain of spheres exchange method. *J. Chem. Phys.* **2011,** *135* (14), 144105.
59. Marenich, A. V.; Cramer, C. J.; Truhlar, D. G., Universal Solvation Model Based on Solute Electron Density and on a Continuum Model of the Solvent Defined by the Bulk Dielectric Constant and Atomic Surface Tensions. *J. Phys. Chem. B* **2009,** *113* (18), 6378-6396.
60. Sankaralingam, M.; Lee, Y.-M.; Karmalkar, D. G.; Nam, W.; Fukuzumi, S., A Mononuclear Non-heme Manganese(III)–Aqua Complex as a New Active Oxidant in Hydrogen Atom Transfer Reactions. *J. Am. Chem. Soc.* **2018,** *140* (40), 12695-12699.
61. Rice, D. B.; Grotemeyer, E. N.; Donovan, A. M.; Jackson, T. A., Effect of Lewis Acids on the Structure and Reactivity of a Mononuclear Hydroxomanganese(III) Complex. *Inorg. Chem.* **2020,** *59* (5), 2689-2700.
62. Rice, D. B.; Jones, S. D.; Douglas, J. T.; Jackson, T. A., NMR Studies of a MnIII-hydroxo Adduct Reveal an Equilibrium between MnIII-hydroxo and μ-Oxodimanganese(III,III) Species. *Inorg. Chem.* **2018,** *57* (13), 7825-7837.
63. Hill, E. A.; Weitz, A. C.; Onderko, E.; Romero-Rivera, A.; Guo, Y.; Swart, M.; Bominaar, E. L.; Green, M. T.; Hendrich, M. P.; Lacy, D. C.; Borovik, A. S., Reactivity of an FeIV-Oxo Complex with Protons and Oxidants. *J. Am. Chem. Soc.* **2016,** *138* (40), 13143-13146.
64. Neese, F., A critical evaluation of DFT, including time-dependent DFT, applied to bioinorganic chemistry. *J. Biol. Inorg. Chem.* **2006,** *11*, 702-711.
65. Muckerman, J. T.; Skone, J. H.; Ning, M.; Wasada-Tsutsui, Y., Toward the accurate calculation of pKa values in water and acetonitrile. *Biochimica et Biophysica Acta (BBA) - Bioenergetics* **2013,** *1827* (8), 882-891.
66. Groff, B. D.; Koronkiewicz, B.; Mayer, J. M., Polar Effects in Hydrogen Atom Transfer Reactions from a Proton-Coupled Electron Transfer (PCET) Perspective: Abstractions from Toluenes. *J. Org. Chem.* **2023,** *88* (23), 16259-16269.

67. Ottenbacher, R. V.; Talsi, E. P.; Rybalova, T. V.; Bryliakov, K. P., Enantioselective Benzylic Hydroxylation of Arylalkanes with H2O2 in Fluorinated Alcohols in the Presence of Chiral Mn Aminopyridine Complexes. *ChemCatChem* **2018,** *10* (22), 5323-5330.
68. Schneider, J. E.; Goetz, M. K.; Anderson, J. S., Statistical analysis of C–H activation by oxo complexes supports diverse thermodynamic control over reactivity. *Chem. Sci.* **2021,** *12* (11), 4173-4183.
69. Maldonado-Domínguez, M.; Srnec, M., Quantifiable polarity match effect on C–H bond cleavage reactivity and its limits in reaction design. *Dalton Trans.* **2023,** *52* (5), 1399-1412.

Tables of Contents Graphic

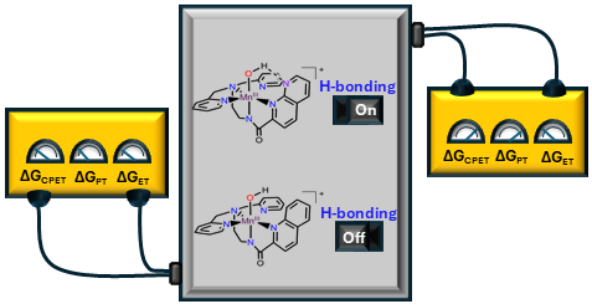

Synopsis

A hydrogen bond to a Mn^{III}-hydroxo complex markedly increases the basicity of the hydroxo ligand, which in turn increases the driving force for concerted proton-electron transfer reactions.